CO2/CH4 Glow Discharge Plasma. Part II: Study of Plasma Catalysis Interaction Mechanisms on CeO2

Carolina A. Garcia-Soto, Edmond Baratte, Tiago Silva, Vasco Guerra, Vasile I. Parvulescu, Olivier Guaitella

CO_2/CH_4 glow discharge plasma. Part I: Experimental and numerical study of the reaction pathways

Edmond Baratte[1], Carolina A. Garcia-Soto[1, 2], Tiago Silva[3], Vasco Guerra[3], Vasile I. Parvulescu[2], and Olivier Guaitella[1,*]

[1]LPP, CNRS, École Polytechnique, Sorbonne Université, Université Paris-Saclay, IP-Paris 91128, Palaiseau, France
[2]Department of Organic Chemistry, Biochemistry and Catalysis, University of Bucharest, Bucharest, Romania
[3]Instituto de Plasmas e Fusão Nuclear, Instituto Superior Técnico, Universidade de Lisboa 1049-001, Lisboa, Portugal
[*]Corresponding author: Olivier Guaitella, olivier.guaitella@lpp.polytechnique.fr

ORCID Numbers:
Olivier Guaitella: 0000-0002-6509-6934
Vasco Guerra: 0000-0002-6878-6850
Tiago Silva: 0000-0001-9046-958X
Carolina A. Garcia-Soto: 0000-0002-3166-530X
Vasile I. Parvulescu: 0000-0002-5519-3423

Acknowledgements

This work was partially supported by the Agence Nationale de la Recherche (ANR, Investissement d'Avenir program), under project ANR-18-EURE-0014. This work was partially supported by the Portuguese FCT-Fundacao para a Ciencia e a Tecnologia, under projects UIDB/50010/2020, UIDP/50010/2020, PTDC/FIS-PLA/1616/2021, EXPL/FIS-PLA/0076/2021. This project has received funding from the European Union's Horizon 2020 research and innovation programme under the Marie Skłodowska-Curie grant agreement No. 813393.

Abstract

A fundamental study of CO_2/CH_4 plasma is performed in a glow discharge at a few Torr. Experimental and numerical results are compared to identify the main reaction pathways. OES-based techniques and FTIR (Fourier Transform Infrared) spectroscopy are used to determine molecules densities and gas temperature. Several conditions of pressure, initial mixture and residence time are measured. The main dissociation products are found to be CO and H_2. The LoKI simulation tool was used to build a simplified kinetic scheme to limit the uncertainties on rate coefficients, but sufficient to reproduce the experimental data. To this aim, only molecules containing at most one carbon atom are considered based on the experimental observations. Obtaining a good match between the experimental data and the simulation requires the inclusion of reactions involving the excited state $O(^1D)$. The key role of CH_3 radical is also emphasized. The good match obtained between the experiment and the simulation allows to draw the main reaction pathways of the low-pressure CO_2-CH_4 plasmas, in particular to identify the main back reaction mechanisms for CO_2. The role of CH_2O and H_2O in the gas phase is also discussed in depth as they appear to play an important role on catalytic surface studied in the part II of this study.

1 Introduction

One of the greatest challenge of the beginning of this century is the struggle against global warming. To limit the anthropogenic emissions which are the main causes of the climate change, it is necessary to reduce the

emission of greenhouse gases. The Dry Reformation of Methane (DRM) is a promising lead in this direction: it recycles CO_2 and CH_4, the main greenhouse pollutants, into value added products:

$$CO_2 + CH_4 \rightarrow 2CO + 2H_2$$

Together, they can be used to provide a form of energy storage through their recombination into heavier hydrocarbons with the Fischer-Tropsch process:

$$nCO + (2n+1)H_2 \rightarrow C_nH_{2n+2} + nH_2O$$

Though DRM can be achieved chemically, using cold plasma represents another interesting path which could play on the non-equilibrium characteristics of these complex media to avoid heating of the mixture and subsequent energy waste ([1, 2, 3]). Extended literature on CO_2 plasma is available ([4, 5, 6, 7]), as well as on CH_4 ([8, 9, 10]). Despite this, the physical basis of CO_2-CH_4 plasmas are still uncharted. A recent effort has been undertaken on the investigation of the main mechanisms occuring in CO_2-CH_4 plasmas, both experimentally and computationally. On one hand, many different discharges were studied experimentally, including nanosecond discharges [11, 12], low pressure RF discharges [13], or high-pressure gliding arc discharges [14]. Finally, numerous studies have used dielectric barrier discharges (DBD) at atmospheric pressure ([15, 16]). However DBDs are often studied in the prospect of applications and therefore often with a catalyst, making the understanding of basic physical phenomena challenging. Indeed, the interactions between a plasma and a catalyst are multiple and are not limited to the mere supply of reactive species produced by the plasma on the surface of the catalyst [17, 18]. The complex materials used as catalysts also influence the plasma dynamics. Studying this interaction in packed-bed DBDs with no access for *in situ* measurements, and generating transient filamentary discharges, does not allow the identification of the different mechanisms really controlling the conversion of CO_2 and CH_4.

On the other hand, a strong modelling effort has also been done for understanding CO_2/CH_4 kinetics: the gliding arc discharge studied in [14] was presented with a complete model of the discharge combining a gas flow approach with a 3D plasma arc model, a particle tracing model and a quasi-1D kinetic model. CO_2-CH_4 DBD discharges at high pressure have been incrementally studied: first with a 1D fluid model of a CO_2-CH_4 plasma in [19] and in [20],whose kinetic scheme was updated for H_2O and N_2 and used in a 0D global model in [21]. The CO_2-CH_4 nanosecond repetitive discharges (NRP) were modelled with 1D fluid model in [22], whose kinetic scheme was modified in [23] to take into account surface processes. Another 1D fluid model taking into account catalytic surfaces and spatial inhomogeneity has been developed in [24] to model a cylindrical packed-bed DBD reactor. Finally, [25] recently developed an neural network based model of a CO_2-CH_4 nanosecond pulsed dielectric barrier discharge to predict the conversion, energy efficiency and selectivity of the discharge, but does not relies on a chemistry set. This model does not offer insights on the CO_2-CH_4 plasmas, but rather predictions for optimizing DRM.
In these modelling works, a complex chemistry including C_2H_Y molecules (and sometimes C_3H_Y molecules) was used, despite these molecules being only minor products. Including these molecules leads to an exponential increase in the number of rate coefficients to include and therefore to a strong increase in the uncertainty of major rate coefficients.

In this work, we use a low pressure glow discharge to serve as basis for validation of a 0D kinetic model including only molecules with up to one carbon atom to bring insights on the key processes allowing conversion in a CO_2-CH_4 plasma. The procedure of comparison of the measurements in the glow discharge with 0D kinetic model coupling electron kinetics and chemistry is similar to what had previously been done for pure CO_2 in [26]. The kinetic scheme developed in [26] was the starting point of this work. The glow discharge is chosen for its reproducibility and homogeneity, ideal for comparison with a 0D model, as well as for the easy experimental access to key quantities of the plasma (the electron density n_e and the reduced electric field E/N). The goal of this study is to provide insights on the basic processes occurring in CO_2-CH_4 plasmas at low pressure by trying to keep the number of reactions relatively small in order to minimize the number of reactions with unreliable rate coefficients. The understanding of the gas-phase kinetics gained in this work will serve as a basis for the analysis of the results presented in Part II of this study [27]. Indeed, part II is devoted to the study of the species forming on the surface of a CeO_2 pellet exposed to exactly the same plasma as the one studied here. The combined study of the plasma phase and the adsorbed phase in the same reactor is indeed essential to identify the mechanisms of plasma/catalyst interaction.

2 Experimental setup

The discharge used for this study is a glow discharge sustained at low pressure (between 1 and 7 Torr). The reactor is made of two identical pyrex cylinders, of inner radius of 1cm, attached together in a shape of an L, as

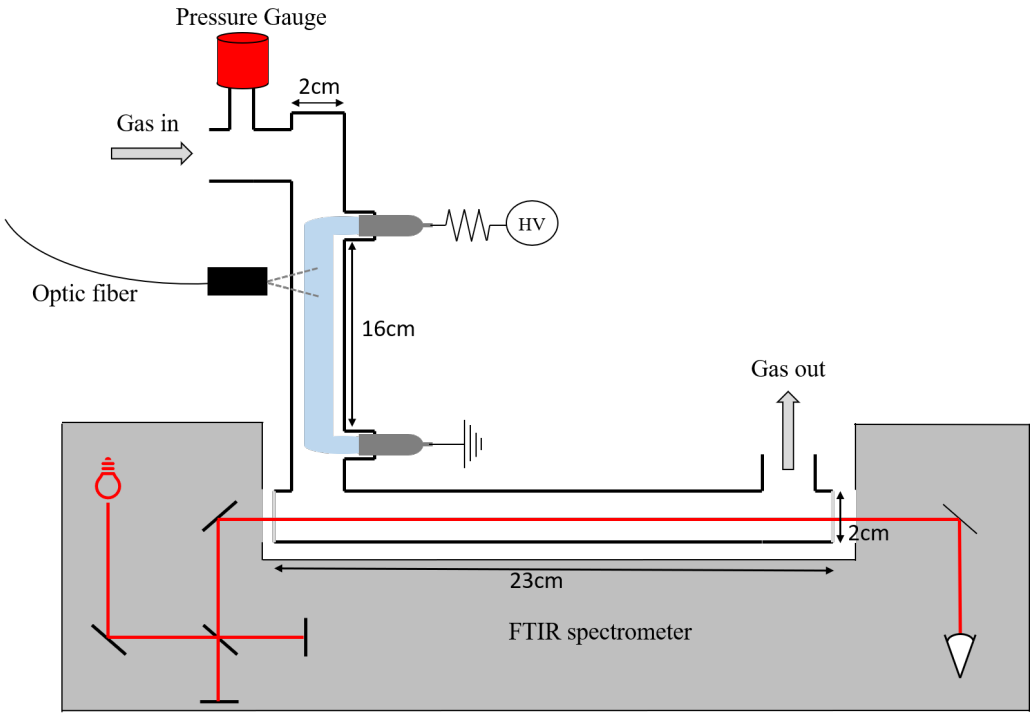

Figure 1: Experimental Setup

visible on fig 1. The L-shape configuration allows for direct measurement of the post-discharge area, assuring that the gas travels only a few centimeters (corresponding to a few seconds for the flows used) between the plasma area and the measurement area. The travelling time is much longer than the recombination processes of excited species ensuring that no reactive species (ions, excited states or radicals) reach the measurement cell. This also ensures that the gas is in contact with nothing else than pyrex between plasma and the measurement point (especially with no metal which could have a catalytic effect). The electrodes are hollow cathodes made mostly of iron and their top surface is protected by an alumina-based ceramic. Therefore, they contain no carbonated compound likely to influence the results of our measurement. Moreover a pure oxygen plasma is used prior to measurements to check that no carbon deposits possibly accumulated during previous experiments generate detectable levels of CO and/or CO_2. Gas is flowed in the reactor with 3 Bronkhorst flowmeters (with an accuracy of 0.1sccm), with a total flowrate kept between 1.85 and 7.4sccm, and pumped by an Edwards XD10 pump. The pressure is measured at the entrance of the reactor by a Pfeiffer pressure gauge. A continuous plasma is turned on in the reactor with a FUG HP 350-6500 Power supply. The reactor is in plug flow configuration, meaning that the gas is continuously supplied and pumped but at a relatively low flow. The total gas flow determines the pseudo steady state (i.e a steady state where dissociation is compensated by gas renewal). The measurement area of the reactor is placed in the sample compartment of a Brucker Vertex 70 FTIR, where the IR spectra can be measured. Optical emission spectroscopy is performed simultaneously: a collimator is used to acquire light from the plasma and sends it through an optical fiber to a Ocean Optics Maya USB spectrometer. The USB spectrometer allow to obtain a spectrum between 250 and 900nm with a resolution of 0.5nm, allowing to clearly observe O and H atomic lines as well as molecular band such as the CO Angstrom band.

For each condition measured, the gas is supplied in the line for 5 minutes before turning on the plasma to ensure a good mixing of the different gases. A first FTIR measurement is taken before the plasma is turned on to check the ratio of initial gases. The initial mixture has been varied between 100:0 and 60:40 CO_2-CH_4, keeping the CH_4 initial fraction low enough to avoid significant carbon deposition on the walls. However, when the plasma is run for a long time (several hours) and for long residence time (5-7 seconds), some deposition is observed near the high voltage electrode. When carbon deposition is observed, the reactor is cleaned with an oxygen plasma until no CO or CO_2 can be measured with the FTIR in the measurement cell. Despite the small carbon deposition, it will be shown further that the carbon balance is nearly fulfilled in the chosen working conditions. Once the plasma is ON, the IR spectrum is measured after 8 minutes, corresponding to the stabilization time of CO_2-CH_4 plasma in our conditions as seen on IR and OES spectra. For each conditions, a steady state of pressure and temperature in the plasma in assumed. Each conditions is measured 4 times in a row, each measurement is an average of 10 IR spectra. All the steps of the acquisition are automated. The list of measured conditions is given in table 1.

Pressure	[1;7] Torr
Current	40mA
Initial CO_2-CH_4 fractions	60:40 / 70:30 / 80:20 / 90:10 / 95:5 / 100:0
Total flows	1.85 / 3.7 / 5.55 / 7.4 sccm

Table 1: Conditions used for the parametric study of chemical conversion in the CO_2/CH_4 glow discharge

Rotational temperature measurement by OES

The optical emission spectra are used to measure the temperature of the plasma through the fitting of the CO Angström band following the method described in [28]. Similarly to previous work dedicated to the study of CO2 plasmas [29], the rotational temperature is assumed to be at equilibrium with the gas temperature. The accuracy of the temperature measurement is limited by the instrumental broadening of the USB spectrometer. Comparisons with the rotational temperature measured in pure CO_2 with FTIR spectroscopy (as described in [29]) showed a relatively good agreement of the two methods, with a discrepancy of only 60K.

Densities measurement by FTIR absorption spectroscopy

An infrared absorption spectrum ranging is measured with the FTIR. The spectrum ranges from 500 cm^{-1} to 5000 cm^{-1}, allowing to observe the bands of all hydrocarbons of interest as well as the IR bands of CO_2, CO and H_2O. The FTIR measurement is done in conditions similar to the ones of [29]: the FTIR beam goes through a 23cm-long measurement cell which allow for a sensitivity limit in the order of 10^{20} m^{-3} for all molecules (which depends on the pressure and the molecule line strength). Because the travelling time between the plasma and the measurement (few s) cell is much longer that the rotational and vibrationnal temperatures relaxation time (a few ms in our conditions [29]), the temperature along the FTIR line-of-sight if assumed to be 300K and all vibrational excitation is assumed to have relaxed. The infrared spectra are fitted with a modified version of the algorithm presented in [29]. The algorithm was previously designed to fit the out of equilibrium vibrational and rotational temperatures and dissociation fraction in CO_2 plasmas. The algorithm is modified to fit individually each molecule in the IR spectrum at equilibrium and draw the density of each species (out of equilibrium data are not available for all species). The densities of CO_2, CO, CH_4, H_2O, C_2H_6, C_2H_4 and C_2H_2 can be measured with a sensitivity of 1‰of the total density ($\sim 10^{20} m^{-3}$). The algorithm has been tested in controlled mixture, i.e in a gas mixture without any plasma.

Measurement of the electric field

The reduced electric field E/N, a key parameter for the understanding of the plasma behaviour has also been measured and was found to be typically around 70 Td. The electric field is measured in the same conditions in an identical reactor which integrates tungsten pins at floating potential in the plasma area. The measurement of the potential at the pins allows to determine the electric field assuming the homogeneity of the electric field across the positive column. Combined with the previous measurement of temperature, this yields the reduced electric field E/N.

3 Experimental Results

3.1 Evolution of the temperature with CH_4

In this work, the influence of three different parameters on the final gas composition are investigated: the pressure, the total flow and the initial gas mixture. In order to represent the variation of measured quantities like gas temperature as a function of all three parameters, color maps are plotted. Figure 2 shows the gas temperature measured by OES with a color scale for different initial percentages of CO_2 in the mixture of CO_2/CH_4 (noted f_{CO2ini} on the X axis) and gas flow (Y axis) for each pressure studied (each subplot). For a given pressure and initial CO_2-CH_4 mixture, the temperature appears to be independent from the flow. This was already observed in pure CO_2 and is due to the characteristic time of gas heating (i.e the time necessary for the plasma to reach a steady temperature by balancing electronic heating, VT processes and losses at the wall), which is much smaller ($\sim$ few ms [29]) than the residence time of the gas in the plasma ($\sim$ few s).
For a given pressure and flow, the temperature decreases with the increase of CH_4 percentage. In these measurements, the current is kept constant at 40mA and the power supply voltage varies by less than 5% over the whole initial mixture variation. This means that the power transferred is relatively constant for all gas mixtures studied. Therefore The temperature decrease is not due to lower heating and must be due to higher heat loss. The main cooling channel in our low-pressure glow discharge is the cooling by heat conduction to

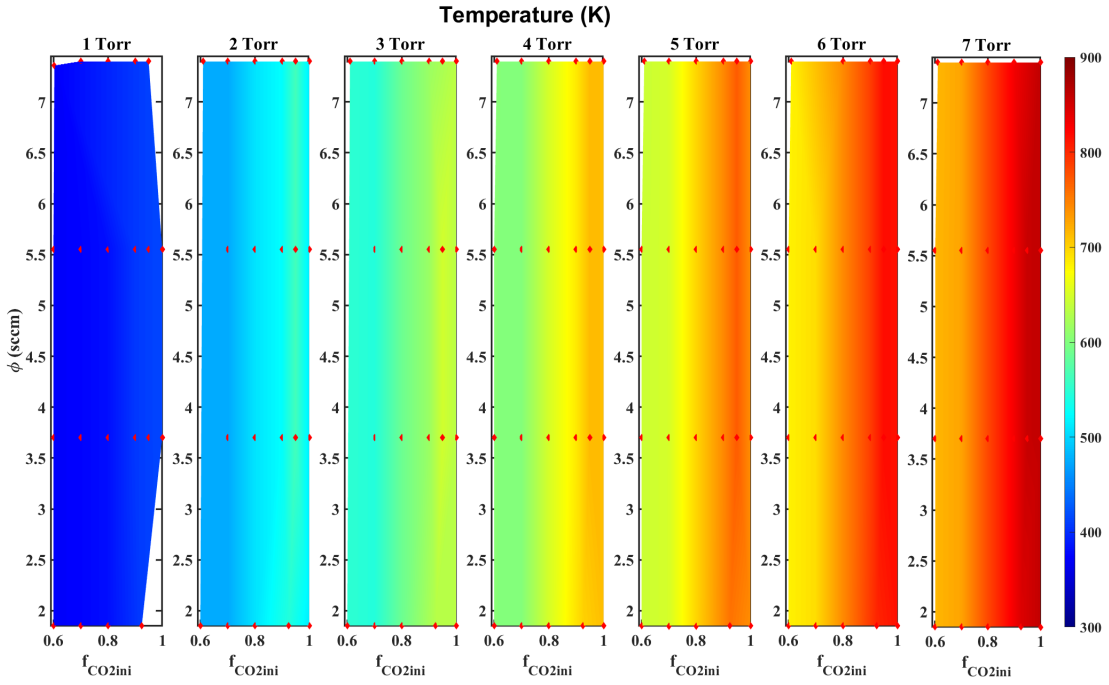

Figure 2: Evolution of the gas temperature obtained by OES in the measured conditions as a function of pressure, initial mixture and residence time. Each image shows for one pressure a colormap of the temperature as a function of the initial CO_2 percentage and of the residence time. The measured points are represented with red squares, while the rest is interpolated. All measurements are taken at 40mA.

the walls as shown in [30] in CO_2 and $CO_2 - N_2$ low-pressure glow discharges. CH_4 has a thermal conductivity twice as high as the CO_2, and H_2 (dissociation product of CH_4) tenfold the one of CO_2. The temperature decrease is therefore attributed to the large thermal conductivity of CH_4 and its by-products like H_2 and the better heat conduction to the walls.

3.2 Evolution of the reduced Electric Field

The evolution of the electric field as a function of pressure measured from the voltage drop in the positive column of the glow is plotted in dashed lines on figure 3 for various CO_2-CH_4 initial percentages. The E field is measured with the pins in the positive column and the temperature is measured with OES. Figure 3 presents the electric field for a flow of 3.7 sccm but the change of flow (and therefore of residence time) has a very small impact on E. The maximum increase when going from 7.4 to 3.7 sccm for a given mixture and pressure is observed at high pressure and is about +4% (from 51V/cm to 53V/cm at 7 Torr at 90:10 CO_2:CH_4). The same order of magnitude is seen at low pressure, with an increase from 25 to 26 V/cm at 2 Torr for the same mixture.
Starting from the pure CO_2 case, the electric field decreases upon addition of 5% of CH_4 in the initial mixture for a given pressure. Upon further addition of CH_4 in the initial mixture, the electric field increases.

The reduced electric field is shown in plain lines on figure 3 for several initial CO_2 percentages. Because it was seen that both the electric field and the temperature are very weakly impacted by the flow, the reduced electric field is also relatively stable with the flow. Contrary to the pure CO_2 case, the reduced electric field does not always decrease with pressure. For low initial CH_4 percentage (95:5 and 90:10 CO_2:CH_4), a decrease is observed with pressure, but the decrease of the 95:5 case (from 73 Td at 2 Torr to 61Td at 7 Torr) is more pronounced that the one of the 90:10 case (from 70Td at 2 Torr to 64Td at 7 Torr). For the 80:20, 70:30 and 60:40 CO_2:CH_4, no clear trend is exhibited and the reduced electric field seems flat with pressure. The trend of the reduced electric field with pressure for initial CH_4 content above 20% can be explained by a competition between two quantities. On one hand, the electric field increases with pressure. On the other hand, the high proportion of CH_4 and its dissociation products lead to better thermal conductivity and stronger heat loss, limiting the temperature increase with pressure. The density increase is therefore stronger than in pure CO_2. The simultaneous increase of E and N with pressure lead to a flat E/N. Nevertheless, the uncertainty of the OES temperature measurement could also flatten the E/N curve with pressure represented on figure 3. Comparison

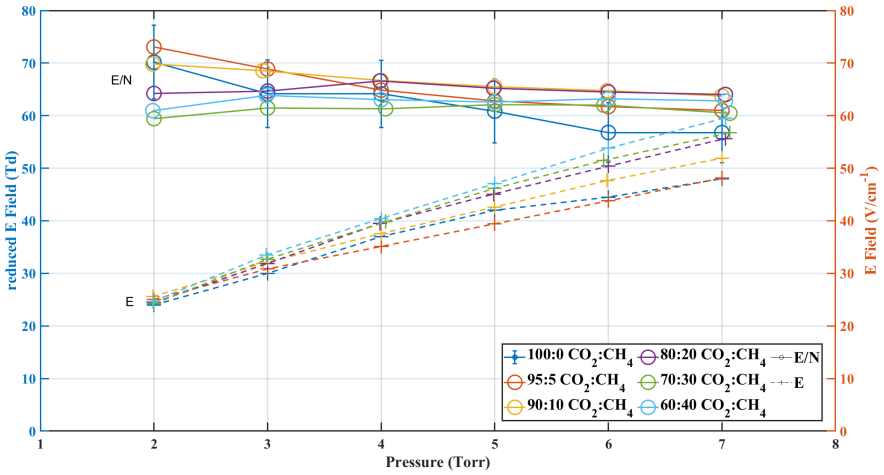

Figure 3: Evolution of the electric field (in dashed lines) and reduced electric field (plain lines) with pressure for various initial CO2%

between OES and FTIR in an additional series of measurement in pure CO_2, where both temperature where temperatures are measured in-situ, showed that the OES tends to underestimate the temperature at low pressure (-20K) and to overestimate at high pressure (∼60K) compared to the FTIR measurements, considered more reliable. If it is assumed that OES temperatures are off by the same amount in CO_2-CH_4 (-20K at 2 Torr and +60 at 7 Torr), the E/N evolution with pressure is not flat anymore and a slightly decreasing trend (similar to CO_2) is observed, though only a few Td between 2 and 7 Torr. The values measured and plotted on figure 3 are the ones kept for the rest of this work.

3.3 Evolution of the main species in the downstream gas mixture

The molecular fractions of several species in the gas (CO_2, CO, H_2, CH_4) are compared here for different pressures. The densities are measured downstream of the reactor and not *in situ*. The densities downstream are comparable to the ones in the plasma because only minor recombination takes place in the post-discharge (as is shown further below). Additional composition measurements by mass spectrometry were carried out further down the gas line (in the far post-discharge, see part II of this work [27]) in the same setup for the same conditions and have shown good agreement with the FTIR measurements. This confirms that little chemistry happens in post-discharge on long time scale (between 2 and 10 seconds after the plasma).
Before detailing each species, a general overview of the plasma composition must be given. While CH_4 seems almost completely dissociated in our conditions, some CO_2 remains. The main products of the CO_2-CH_4 low pressure glow discharge are CO and H_2, as often reported for CO_2-CH_4 discharges ([11] for NRP, [31] for atmospheric glow, or more recently in a GA discharge [14]). In this work, water is obtained as well (up to 15% of the gas density). C_XH_Y molecules are found only in traces. When heavier hydrocarbons are found here (by FTIR also confirmed by mass spectrometry), C_2H_6 is the dominant one, whereas C_2H_2 is usually reported as the main C_XH_Y molecule with X>1 in literature ([11, 14]). Little O_2 (deduced from O atom balance) is found downstream if the CH_4 percentage is above 10%: in a 90:10 mixture at 3 Torr, the O_2 fraction is typically around 5%, and drops below 1% in the 80:20. No O or H atoms are expected downstream because their characteristic recombination time at the wall is much shorter (respectively tens of ms and ms) than the time it takes for the gas to travel from the reactor to the measurement cell.
Similarly to the temperature maps, the fraction of the main species in the gas mixture downstream the plasma are plotted versus the initial % of CO_2 and versus the total gas flow for each pressure in the following figures (4,5,6 and 7). For more readability, an interpolated surface is plotted in colour, while the measurement points are plotted as red diamonds. The number of point for the interpolation is chosen so that the interpolant gives the measured values at the measured conditions.

The CO_2 fraction in the plasma is shown on figure 4. For all pressures and residence times, the CO_2 fraction strongly increases when changing from 100:0 to 95:5 CO_2-CH_4, before going back down when increasing the CH_4 content. This phenomenon, which translates by a red band very visible between 2 and 7 Torr, is less clear at 1 Torr. For a given pressure, the CO_2 fraction decreases with the residence time (as expected due to longer exposure to electron impact processes). Hence for a given pressure, CO_2 is always minimal at high CH_4 percentage and low flow (high residence time), while it is always maximum at 95:5 CO_2-CH_4. The value

of the minimum final fraction is however stable for all pressure, remaining at 15% of the total density, while the maximum fraction of CO_2 increases from 1 to 3 Torr before stabilizing at approximately 70% of the total plasma density.

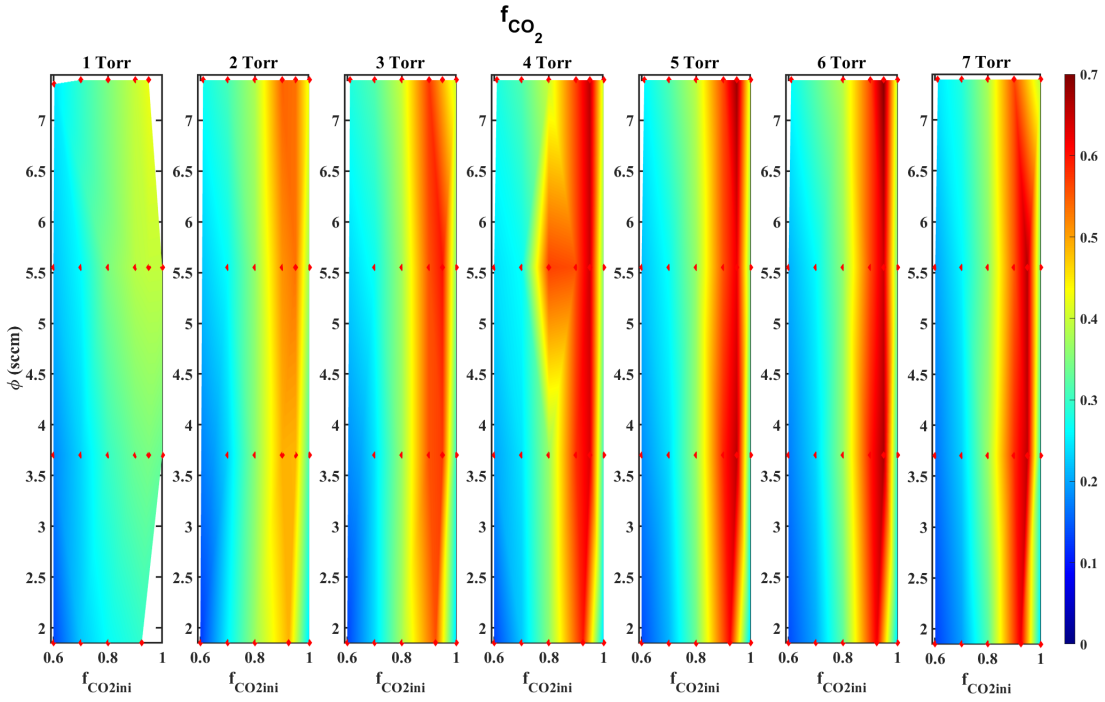

Figure 4: Evolution of the fraction of CO_2 in the measured conditions as a function of pressure, initial mixture and residence time. Each image shows for one pressure a map of the CO_2 final fraction as a function of the initial CO_2 percentage and of the residence time. The measured points are represented with red squares, while the rest is interpolated. All points are taken at 40mA

The CO fraction in the plasma is represented on figure 5. For a given pressure, the CO fraction is maximal for low flow (high residence time) and high initial CH_4 %. For pressures between 2 and 7 torr, the CO fraction shows a drop of almost a factor 2 when changing from 100:0 to 95:5 CO_2-CH_4, then goes back up upon addition of more methane in the initial mixture, mirroring the previously shown CO_2 fraction on figure 4. This is visible for all measured residence times. For a given pressure and initial CO_2-CH_4 mixture, the final CO fraction increases with the residence time. The large fractions of CO observed ($\sim$25% at f_{CO2ini}=0.6 for instance) show that a large part of the CO comes from oxidation of CH_4 and not only from the dissociation of CO_2.

CH_4 is efficiently converted, with little to no CH_4 remaining. The final CH_4 fractions, represented on figure 6, show a linear trend with the initial CH_4 fraction and with the residence time: CH_4 is fully dissociated at low initial CH_4 percentage and at low flow (high residence time). The behavior of CH_4 is similar for all pressures: around 10% remain in the case 60:40 CO_2:CH_4 for all pressures and for high flows (7.4sccm, top right corner of the maps). Increasing the residence time in the same mixture leads to final CH_4 percentage close to 4%. For any other mixture, the final amount of CH_4 is decreased below 1% for all residence times.

H_2 is not directly measured by FTIR because it is not IR active. The fraction of H_2 in the plasma is therefore deduced from H atoms balance assuming that all non-detected H atoms are recombined into H_2. The values found with this method are in good agreement with mass spectrometer measurements even though the error bars of MS for H_2 are rather large. The fraction of H_2 in the gas represented on fig 7 increases with the initial CH_4 percentage and with the residence time at a given pressure. The H_2 fraction is thus always maximum on left side of the maps for any pressure. The maximum fraction of H_2 is relatively stable with pressure, remaining in the range 32-45% of the total gas density, with a peak at 4 Torr.

The fraction of water (which is measured by FTIR but not represented here) has a limited range of variation. For 5% of initial CH_4, approximately 5% of water is formed for all residence times and all pressures. This amount increases slightly when more CH_4 is added but remains between 8% (for low residence times) and 11% (for higher residence time).

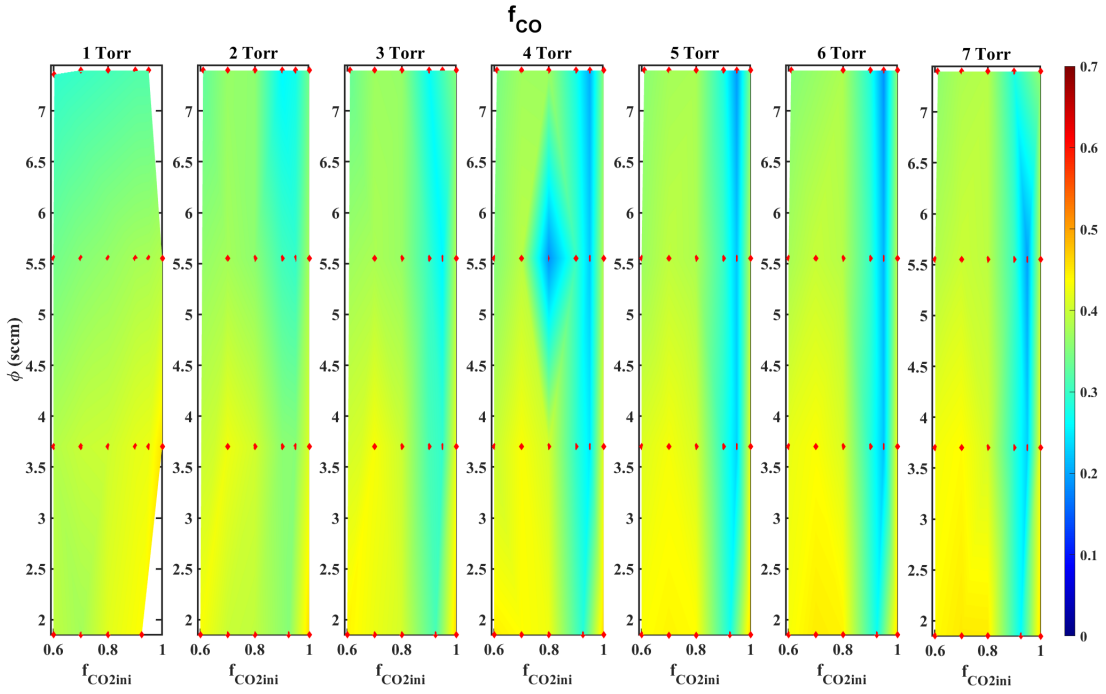

Figure 5: Evolution of the fraction of CO in the measured conditions as a function of pressure, initial mixture and residence time

The fraction of O_2 is not represented here as it falls to 0 when the initial CH_4 content is higher than 10%. Similarly to H_2, O_2 is not measured directly but deduced from the O atom balance assuming that all O atoms missing from the balance are recombined into O_2. Traces of C_2H_6, C_2H_4 and C_2H_2 are found but are negligible (their sum account for less than one percent in the best case). Despite the weak densities, it is worth noting that C_2H_6 peaks at 1 Torr, suggesting that surface processes could be at play here, while C_2H_4 systematically peaks in the 60:40 CO_2-CH_4 case and always at high flow. The high flow corresponding to a short residence time in the plasma, this suggested that C_2H_4 could be an intermediate in the chemistry, destroyed on long time-scales.

The deposition of carbon on the walls of the reactor has been computed as well using the carbon balance and assuming the missing carbon was all deposited on the wall in the form of pure carbon. The result of this estimation is plotted on figure 8. The carbon deposition starts once CH_4 reaches 30% of the initial mixture and is stronger at lower flow. In the most critical case (60:40 CO_2:CH_4 at 4 Torr), less than 15% of the total C atoms are lost. In most cases, the deposition remains around 10%. The percentage of C atom deposited being low enough, the deposition will be neglected for further analysis.

3.4 Estimation of the atomic densities by actinometry

The atomic O and H species have a strong influence on the chemistry and can thus play a key role in the plasma. An estimation of their densities is therefore crucial to understand the plasma mechanisms. The absolute densities of atomic H and O in the plasma are measured by actinometry, following the method presented in [32]. The atomic lines of oxigen atoms at 777 nm (writen O777 in the following) and at 845 nm (O845) are used for the computation of O atom density.The H_α line at 656 nm (H656) was used for H density. 5% of Ar was introduced in the gas flow (in a dedicated series of measurements) to serve as actinometer. The Ar750 line is used for the line ratio. The spectral sensitivity of the USB spectrometer was calibrated with a calibration lamp (Ocean optic DH3-Plus) over the whole visible range. The actinometry equations for O with Ar actinometer yield:

$$[O] = \frac{I_O}{I_{Ar}} * \frac{k_e^{Ar}}{k_e^O} * \frac{a_{Ar}}{a_O} * [Ar] \quad (1)$$

where I_X is the intensity of the line emitted by X, k_e^X the rate coefficient of electronic impact excitation of the species X radiating the line studied and a_X is the effective branching ratio of the studied transition. The O line intensity drops with small amount of CH_4. Using eq 1, the fraction of O atoms is estimated to reach 15% in pure CO_2. However it falls to 4% of the gas density in the 95:5 CO_2:CH_4 plasma and 1 percent of the gas

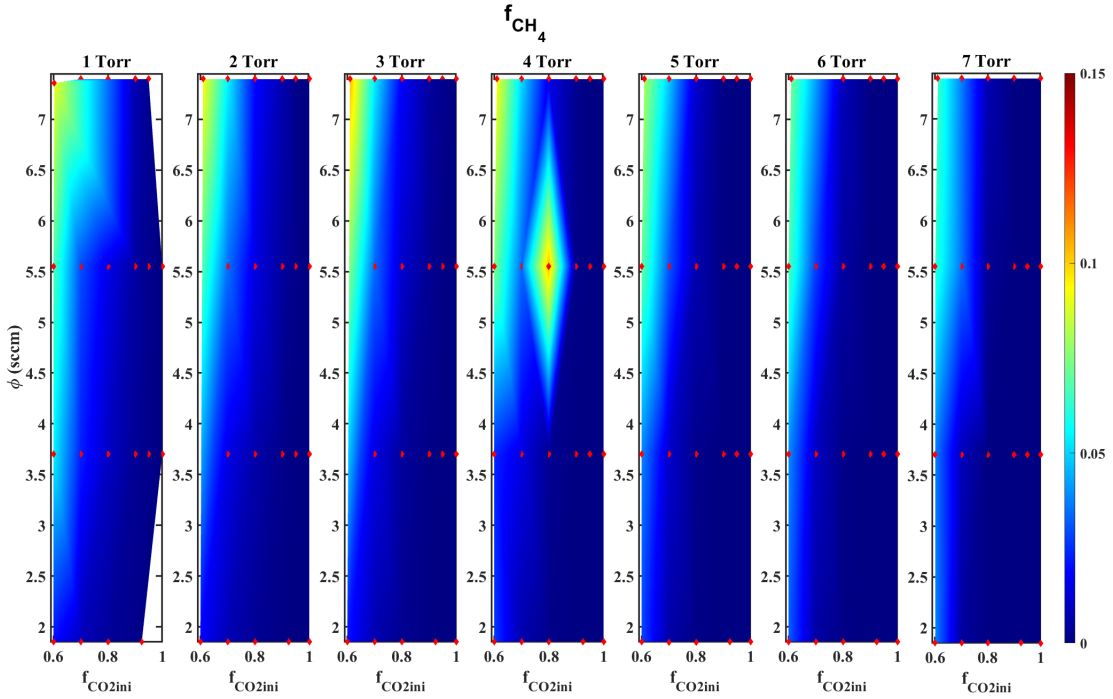

Figure 6: Evolution of the fraction of CH_4 in the measured conditions as a function of pressure, initial mixture and residence time

density in the 90:10 CO_2:CH_4 case. When CH_4 makes up for more than 10 % of the initial mixture, the O line is below noise level. Because of this, the ratio $\frac{I_O}{I_{Ar}}$ is close to 0 for initial CH_4 content above 10% and it is estimated that the atomic O makes up for less than 0.1% of the total mixture in these cases. For initial CH_4 content above 10%, the O atoms are not considered to be a major species.
Though the H line is convoluted with a larger emission band from the CO Angström system which can account for up to 20% of the intensity, it is nonetheless possible to see the evolution of the line, whose intensity increases with the CH_4 content. The H density is computed following the same method as for O densities. The role of dissociative excitation ($e + H_2 \rightarrow e + H + H(n = 3)$)was found to be negligible. Indeed, Using the actinometry hypothesis, the intensity is indeed given by :

$$I_{H656} = C_{656} * h\nu_{ij}^H * (k_e^H * [H] + k_{DE} * [H_2]) * n_e * \frac{A_{ij}^H}{\sum A_i^H + \sum_Q k_Q^H [n_Q]} \tag{2}$$

$$= C_{656} * h\nu_{ij}^H * (k_e^H * [H] + k_{DE} * [H_2]) * n_e * a_{ij}^H \tag{3}$$

$$\tag{4}$$

where C_{656} is a constant depending on the experimental setup, ij correspond to the upper and lower levels of the transition radiating the 656nm line, k_e^H the electronic excitation rate coefficient, k_{DE} the dissociative excitation rate coefficient, n_e the electron density, n_H the atomic hydrogen density and a_{ij}^H the efficient branching ratio of the transition. The ratio $\frac{k_e^H}{k_{DE}}$ was computed for a 60:40 CO_2:CH_4 mixture at various pressures using the LoKI B solver (Lisbon Kinetics solver,[33]) and the composition, temperature and reduced electric field measured above. The ratio was found to be close to $4{\times}10^3$ in our conditions. Neglecting dissociative excitation, the H atom density was computed

$$[H] = \frac{I_H}{I_{Ar}} * \frac{k_e^{Ar}}{k_e^H} * \frac{a_{Ar}}{a_H} * [Ar] \tag{5}$$

Using the coefficients given in table 2, this estimation yields that for an initial CH_4 content of 30%, the atomic H density should remain below 1% of the total mixture. Because $k_e^H * [H] >> k_{DE} * [H_2]$, the hypothesis of neglecting the dissociative excitation is consistent. The atomic H density computed here is only an order of magnitude because the basis of the line is convoluted with the CO Angstrom band which prevents exact calculations.

In the following sections, a kinetic scheme is developed to propose a model that accounts for each of these experimental observations.

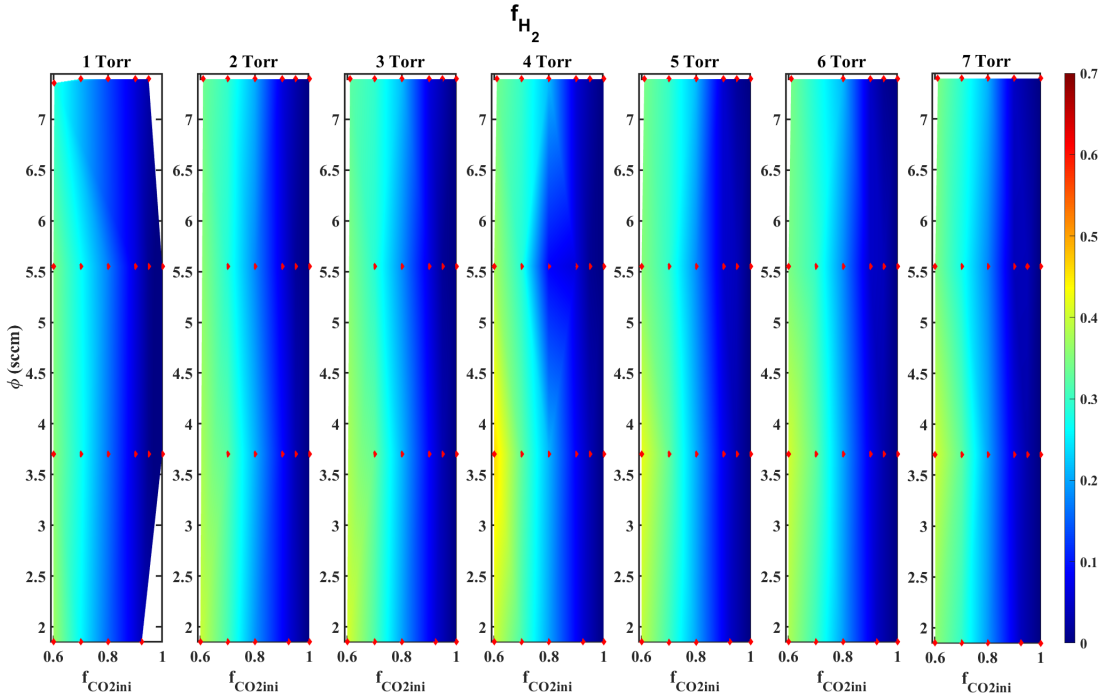

Figure 7: Evolution of the fraction of H_2 in the measured conditions as a function of pressure, initial mixture and residence time

species	Wavelength (nm)	Emitting State	A(s^{-1}) [34]	$k_Q(m^3.s^{-1})$ averaged over all quenchers
Ar	750	2P1	4.5×10^7	7.6×10^{-16} [32]
H	656	Alpha	6.45×10^7	2.5×10^{-15} [35]
O	777	^{3}P5P	3.69×10^7	10.6×10^{-16} [36]
O	844.6	^{3}P^{3}P	3.69×10^7	9.4×10^{-16} [37]

Table 2: Values of the coefficient used for actinometry calculations

4 Modelling

4.1 Overview of the LoKI simulation tool

Because the number of possible interactions in a CO_2-CH_4 plasma is too large to draw a simple chemical scheme from the experimental results, the measurements done in the glow discharge are compared with a 0D kinetic model. The Lisbon Kinetic simulation tool (LoKI) is used both for solving the Boltzmann equation and for the 0D chemical solver [33, 38]. The solver takes as input an initial composition, a temperature, a pressure, an electron density and a guess value of the reduced electric field and computes a final composition and a reduced electric field. The functioning of this solver was previously detailed in [26] for similar work on pure CO_2. In a few words, after providing the working conditions of pressure and temperature (as well as a set of electron impact excitation cross-sections and chemistry rate coefficients), the EEDF is first computed by solving the Boltzman equation using guess values of E/N and n_e. After, the rate balance equations are solved for all heavy species in the plasma:

$$\frac{\partial n_s}{\partial t} = \sum_i (C_{s,i} - D_{s,i})$$

where n_s is the density of the species s, and $C_{s,i}$ and $D_{s,i}$ are respectively the creation rate and destruction rate of species s in reaction i. The electron kinetics and chemistry solver are run iteratively so that the value of the E/N used ensures quasi-neutrality of the plasma. An additional loop ensures that the electron density provided matches the experimental current. At the end of the global cycles of LoKI, the current is recomputed from the electron density, the electron mobility (obtained from the Boltzmann solver) and the reduced electric field:

$$I = n_e * \pi r^2 * q * E/N * \mu_{red} \quad (6)$$

where I is the current, r the radius of the tube, q is the charge of the electron and μ_{red} is the reduced mobility. In this work, a tolerance criterion of 1mA is chosen. If $|I_{exp} - I_{sim}| > 1mA$, the electron density is modified

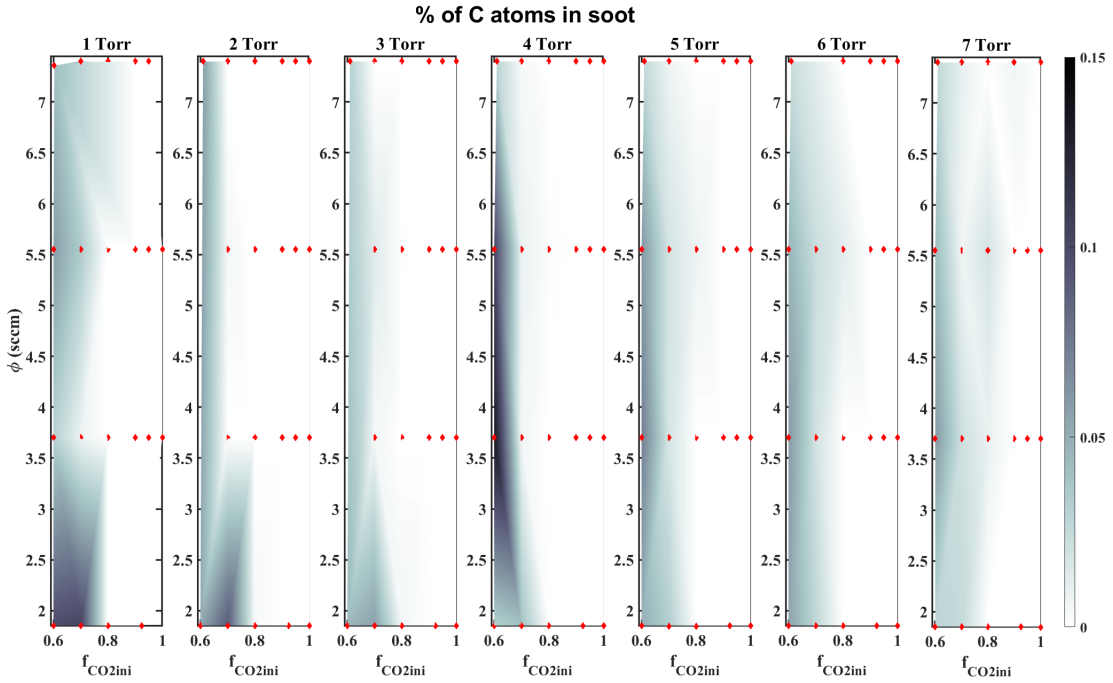

Figure 8: Fraction of C atoms lost in carbon deposition at the walls

and the whole process is run again. The simulation tools gives in the end a complete overview of the plasma parameters (EEDF, electron density, self-consistent reduced electric field and density of all the species included in the model) in the stationary state, as well as the evolution of densities between ignition of the plasma and steady state.

4.2 Resolution of the Boltzmann equation for the electron kinetics

The EEDF is computed by the Boltzmann solver of LoKI, which has already been extensively described ([33] and [38]). As CO_2, CO, O_2, CH_4, H_2 and H_2O are the main products, it is assumed that the EEDF in the plasma can be well described by using only these molecules in the Boltzman solver. It would not necessarily be an improvement to use more species, as they often do not have a set of complete and consistent cross-sections validated against the swarm parameters. Including other species in the EEDF would result in minimal change for the EEDF and would bring more uncertainty because of the validity of the sets employed.

The CO_2, CO, O_2 and O sets of cross-sections were taken from [26], whose work in pure CO_2 serves as basis for the kinetic scheme presented in this work. The cross-sections sets used in [26] were taken from the IST Lisbon database on LXCat. For vibrational processes, the molecules are assumed to follow a Boltzmann distribution at T_{vib}=T_{gas}. The various processes included in the sets on the IST-Lisbon LXCat sets were described in [39] for CO_2, in [40] and in [41] for O_2 and O and in [42] for CO. For the computation of the EEDF, elastic collisions, electronic excitation, vibrational excitation and dissociation are included in the sets. The water cross-sections are taken from [43], where a set of complete and consistent H_2O cross-sections validated against the swarm parameters was made publicly available for the first time. The CH_4 cross-section are taken from [44]. Two complete and consistent sets of cross-section validated against swarm parameters are available for CH_4 to our knowledge: [45] (IST Lisbon database) and [44] (Community database). The choice of [44] was made for several reasons: first, this sets includes more dissociation cross-sections of CH_4, which in turn will give a better picture of the chemistry. Second, this set does not include any fitted cross-section (cross-section gathering several unknown processes fitted to match the swarm parameters). This avoids mixing two reactions in the same cross-section, making it easier to reuse the same set for the chemistry part.

4.3 Chemical kinetic scheme

The chemistry set is an input of the chemistry solver, independent of the input of the sets of cross-sections provided for the computation of the EEDF. It consists in a set of reactions along with their rate coefficients (which can be temperature dependent). Two types of reactions can be included: reactions involving electrons whose rate coefficient are calculated from the EEDF and provided cross-sections, and chemical reactions whose

	neutral species	ions	excited states
Pure CO_2 case (validated in [26])	CO_2, CO, O_2, O	CO_2^+, CO^+, O_2^+, O^+, O^-	$CO(a^3P)$, $O(^1D)$, $O2(b^1S_g^+)$, $O2(a^1D_g)$
Species added in the simplified CO_2-CH_4	CH_4, CH_3, CH_2, CH, H_2, H, OH, H_2O, HCO, CH_2O	CH_4^+, CH_5^+, CH_3^+, CH_2^+, CH^+, H_2^+, H^+, H_3^+	

Table 3: List of species included in the chemistry scheme of the model

rate coefficients must be provided.
The pure CO_2 part of the chemical kinetic scheme, which was previously developed in [26], was completed with CH_4 and by-products reactions. Because it was found experimentally that the molecules with two carbon atoms are only a minor product of the plasma, the C_2H_Y molecules were neglected to limit the complexity of the model and minimize the errors made by adding unessential reactions with uncertain rates. The list of species included in the model are presented in table 3. In [26], the vibrational chemistries of CO_2, CO and O_2 were taken into account for the computation of the EEDF but not for the chemical part (the rates of vibrational excitation were simply not included in the chemistry solver), which still yielded good agreement between experimental dissociation and simulated one. The same choice is done in this work and is applied to CH_4 and water, whose vibrational excitation is removed from the chemistry set. Several reasons justify this choice. First, measurements of the vibrational excitation of CO_2 and CO in a CO_2-CH_4 discharge show that CO and CO_2 vibrational excitations are very efficiently quenched by CH_4 and its by-products, leading to vibrational temperatures lower in CO_2-CH_4 than in pure CO_2. Second, recent studies on the vibrational relaxation of CH_4 have shown that the VT processes take place on a very short time-scale ([46]), leading to think that no vibrational excitation of CH_4 can build-up in our plasma and that the population of vibrationally excited CH_4 in the plasma is negligible. Third, the rates coefficients of VV and VT processes between vibrationally excited CO_2 or CO and the various by-products of CO_2-CH_4 mixtures are very poorly known, with values in literature ranging over several orders of magnitude ([47, 48]), making it difficult to accurately simulate the populations of the various levels. Note that a model accounting for the vibrational kinetics of CO_2 and CO was recently presented in [49].
For the CO_2-CH_4 chemistry including only single-carbon molecules, the added chemistry totalizes 140 neutral-neutral reactions, 40 electron impact reactions and 40 ion-neutral reactions. All the reaction rates coefficient with their sources are given in the supporting information. Most of the rate coefficients are taken from the NIST chemical kinetic database for the neutral species chemical reactions or from the UMIST database for the ionic reactions.When possible, rate coefficients whose original temperature range matched the present temperature range were privileged. However, because of unavailability of a rate coefficient in the correct temperature range, many reactions use rate coefficients out of the temperature ranges given in their original literature. Most of the ions were included because they could be obtained straight from electron impact on one of the major molecules of the plasma (CH_4, H_2 or H_2O). CH^+,H^{3+} and CH_5^+ were believed to play an important role in the plasma according to previous CO_2-CH_4 modelling in literature ([22]). The kinetic scheme also includes inflow and outflow reaction as done is [26].

4.4 Diffusion and Recombination of atomic species at the walls

In the model, the diffusion and recombination of atomic species at the wall is taken into account. The recombination of atomic O into O_2 and of atomic H into H_2 are considered using the reactions :

$$O + wall \rightarrow \frac{1}{2}O_2 \tag{7}$$

$$H + wall \rightarrow \frac{1}{2}H_2 \tag{8}$$

The characteristic loss frequency of a species ν_s at the wall is given by

$$\nu_s = \frac{\Lambda^2}{D_s} + \frac{V}{A} * \frac{4 - 2\gamma_s}{\gamma_s v_{ths}} \tag{9}$$

where V/A is the ratio of the reactor's volume over area, v_{th} the thermal velocity, γ_s the probability of loss, Λ the characteristic diffusion length and D the diffusion coefficient [50] . In a cylindrical reactor of length L and radius R, Λ is given by

$$\frac{1}{\Lambda^2} = (\frac{2.405}{R})^2 + (\frac{\pi}{L})^2 \tag{10}$$

$$\sim (\frac{2.405}{R})^2 \text{ if L } \gg \text{ R} \tag{11}$$

D is the diffusion coefficient computed according to [51]. One of the hypothesis of this model is the value of the atomic recombination probability. For Oxygen, the recombination has arbitrarily been chosen equal to the one in pure CO_2 at 2 Torr (γ_v=10^{-4}), measured in [32]. However, the oxygen recombination probability has a limited impact in the calculation because the atomic oxygen density is expected to be negligible for cases with an initial CH_4 content higher than 10%. The recombination of H atoms at the wall is expected to be more important, though only a small amount of H is present in the plasma. Few works in literature are dedicated to the H recombination on a pyrex wall but the atomic H is expected to be very short-lived due to very fast recombination at the wall. In [52], the loss probability of atomic H in a quartz tube at pressures between 1 and 5 Torr is found to be one order of magnitude higher than the one for O measured in [32]. Previous calculations carried out in [53] support the hypothesis of a large recombination probability. The H recombination at the wall is therefore fixed one order of magnitude higher than the one of O_2, with a γ_H at 0.002. The effect of the recombination probability is investigated further in section 5.5.

5 Comparison of modeling and experimental results

5.1 General Comparison

It is shown *a posteriori* by the model that the composition *in situ* is very close to the composition downstream due to limited reactions in the post-discharge. This is due to the low density of reactive species (such as radicals or excited states) in the plasma. We therefore compare *in situ* simulations and downstream measurements.

A set of reactions concerning all the species from table 3 was assembled and is given in the supplementary information. The model was first implemented using only rate coefficients from literature. The validation of the kinetic scheme proposed here is done through comparison of the measured quantities from the plasma (E/N and densities of the main species) with the simulated ones. The charged particles part of the schemes is assessed first through comparison of the measured E/N (with the electric field from the pins and the gas temperature from the OES) with the E/N calculated self-consistently (from the quasi-neutrality cycle) in LoKI. This comparison allows to validate the kinetics of charged particles as well as the transport theory used. The electron kinetics part of the scheme is assessed first through comparison of the measured E/N (with the electric field from the pins and the gas temperature from the OES) with the E/N calculated self-consistently (from the quasi-neutrality cycle) in LoKI. It is the most direct way to check the good description of the electron kinetics in our model.

The reduced electric field from LoKI is compared to the experimental one on the first graph of figure 9 for a pressure variation at a flow of 1.85 sccm and in a 60:40 CO_2:CH_4 mixture. The simulation clearly shows a trend not visible in the experiment: the simulated E/N increases with decreasing pressure while the experimental one stays steady. The experiment-simulation difference is about 8 Td at 7 Torr but it increases as the pressure decreases, reaching 17 Td at 2 Torr. The gap at 1 Torr is about 25 Td and the insights obtained from the model at this pressure should therefore be taken with caution. Several hypothesis could explain this inconsistency. For example, if the diffusion of the charges to the wall at low pressure is not well accounted for, the global charge could be ill-estimated. The choice of the diffusion scheme made for the charge diffusion to the wall (effective ambipolar diffusion as in [26]) could hence increase the electric field, which is likely to be the main reason of the difference. In order to improve the results related to the reduced electric field, future work can be dedicated to the study of different transport theories presented in [54]. However, surface phenomenon could also play a role in the inaccuracy of the E/N. Indeed, surface processes become very important at 1 Torr [32] and unaccounted processes could affect the chemistry. Because of the relatively large discrepancy in the computed reduced E field, the case of 1 Torr will not be discussed in the next section.

The second graph of figure 9 shows the electron density variation. The electron density increases with pressure but in a limited range. Finally, the 3rd graph of figure 9 shows the simulated ion densities normalized by the electron density. Over the whole pressure range, the main ion is CH_4^+, as opposed to what can be found in literature (which is discussed in section 5.4), and accounts for almost 99% of the electron density. The O^- ion, the only negative ion included in the model, only makes up for 0.1-0.5% of the electron density, which confirms that the plasma can be considered electropositive and that the effective ambipolar diffusion scheme can be applied [26]. The relatively good agreement between the experimental and simulated E/N above 1 Torr ensures a proper description of the electron kinetics in this range which gives confidence in looking now at the densities of the main neutral species.

The main species (CO_2, CO, CH_4, H_2 and H_2O) are compared in the same condition (1.85 sccm and 5 Torr with a mixture variation) on figure 10. The first graph on the left shows the CO and CO_2 densities, simulated in dashed lines and experimental in plain lines. The two species are well predicted both in trends and value. On the second graph, there is an overall fair agreement between model and experiment for the densities of

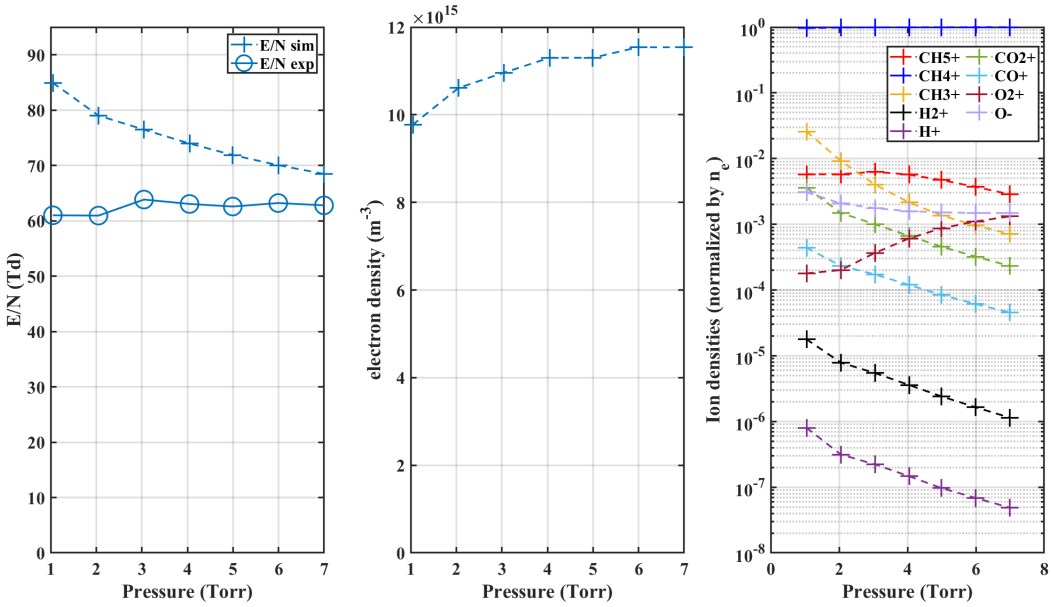

Figure 9: Electron kinetics for a pressure variation at 1.85 sccm in a 60:40 CO_2:CH_4 mixture. The simulated and experimental reduced electric field are compared on the first graph. The evolution of the electron density and ion densities are plotted next. The simulation is plotted in dashed lines and the experiment in plain lines

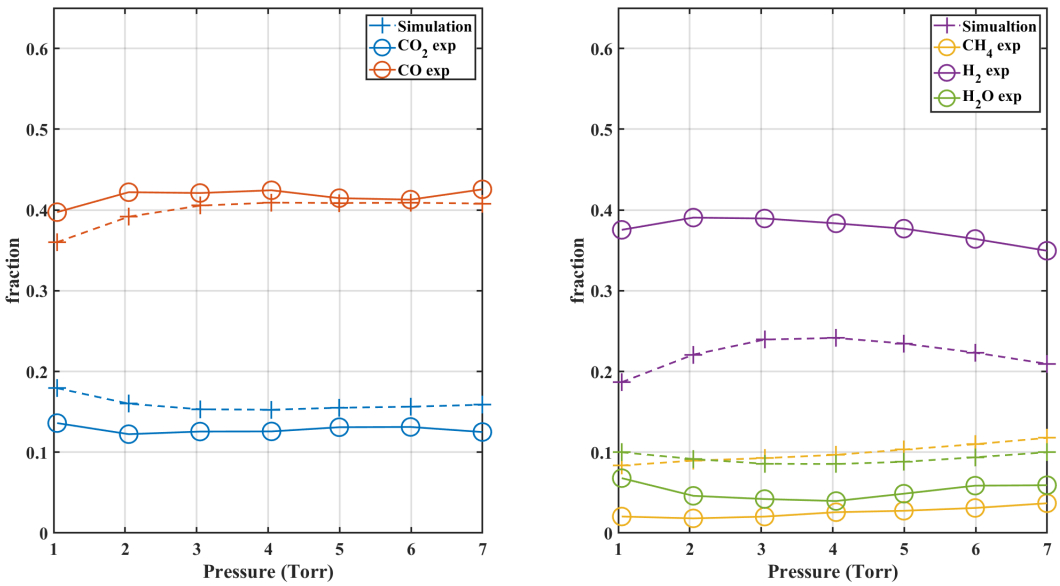

Figure 10: Comparison of the simulation and the experiment for a pressure variation at 1.85 sccm in a 60:40 CO_2:CH_4 mixture. The simulation is plotted in dashed lines and the experiment in plain lines

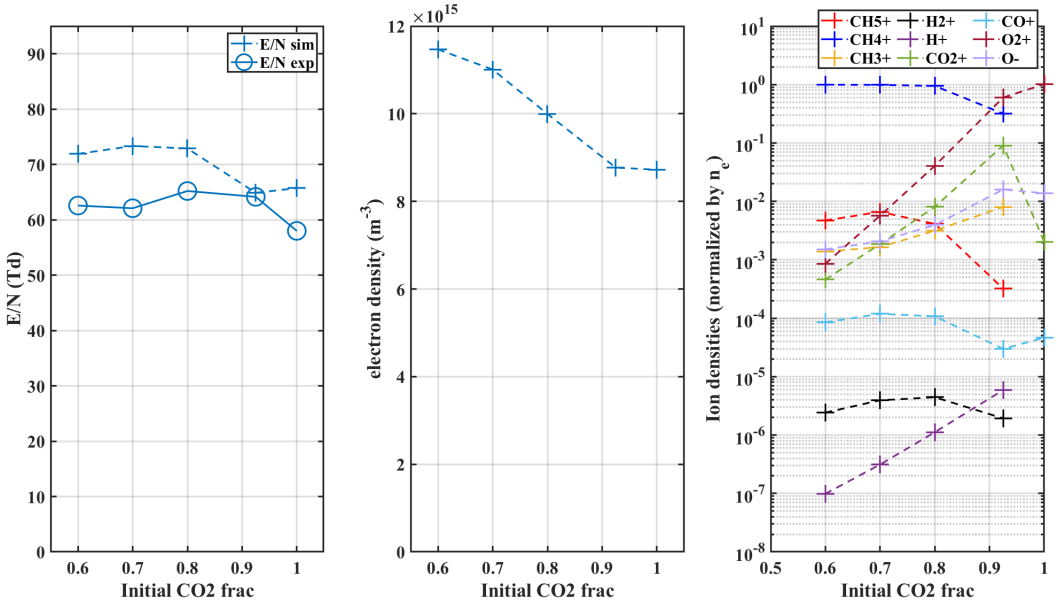

Figure 11: Electron kinetics for a mixture variation at 1.85 sccm and 5 Torr. The simulated and experimental reduced electric field are compared on the first graph. The evolution of the electron density and ion densities are plotted next. The simulation is plotted in dashed lines and the experiment in plain lines

the other species, but several discrepancies are worth pointing out. The calculated CH_4 follows the same trend as the experimental CH_4, but is too high by a factor close to 3 on the whole pressure range. The CH_4 dissociation is underestimated in the model. The H_2 simulated density (in purple) shows a trend different from the experiment: though they both go through a maximum, it happens at 2 Torr in the experiment while it is shifted at 4 Torr in the simulation. The simulated values of H_2 fraction are very far from the experimental ones, with the simulations being too low by a factor 1.5 (with a peak value at 24% versus 37% in the experiment). Finally the simulated water density (in green) shows a good trend but is overestimated by a factor 2. This is surprising as an under-dissociation of CH_4 would predictably leave less hydrogen available to form water.

The following figure 11 shows the comparison between experiment and simulation for a mixture variation: the flow is kept at 1.85 sccm and the pressure is fixed at 5 Torr (where $|E/N_{sim} - E/N_{exp}|$ ~8 Td). This time, the agreement of the calculated self-consistent E/N compares well with the experimental one, keeping on the whole range of explored mixtures $|E/N_{sim} - E/N_{exp}|$<12 Td. The electron density is plotted on the second graph of figure 11 and increases with initial CH_4 content. The electron density does not vary much between the 95:5 and the 100:0 CO_2:CH_4, just like the simulated reduced electric field. The main ion, O_2^+ in pure CO_2, quickly changes to CH_4^+ upon admixture of CH_4: at 5% of CH_4 in the initial mixture, CH_4^+ already accounts for 30% of the total ion density, and rises to close to 100% in the 80:20 mixture. This is likely due to the difference in ionization energy of the molecules. The ionization energy of CO_2, CH_4 and O_2 are respectively $\epsilon_{ionization}(CO_2) = 13.77$ eV, $\epsilon_{ionization}(CH_4) = 12.6$ eV and $\epsilon_{ionization}(O_2) = 12.06$ eV. In pure CO_2 plasmas, O_2 is the easiest molecule to ionize. Its density however drops upon admixture of CH_4 in the plasma, as seen in section 3.3. CH_4 then becomes the easiest molecule to ionize, making CH_4^+ the main ion.

The densities of the main species are shown on figure 12. Just like for the pressure variation, the CO_2 and CO are well reproduced, both in trends and in values. The peak in CO_2 (and the corresponding deep in CO), visible on the CO_2 maps 4, are also reproduced. Concerning the hydrogenated species, the same conclusions are drawn as in pressure variation: CH_4 is under-dissociated, with a density overestimated on the whole range by a factor 3, leading in turn to an underestimated H_2 fraction. The H_2 fraction is underestimated by a factor 1.5. Once again, the water trend is reproduced, going through a maximum at 80:20 CO_2:CH_4 in both the simulation and the experiment, but the simulated values are overestimated.
The simulated CO and CO_2 show relatively good agreement with the experimental values both in pressure and initial mixture variations, but the hydrogenated species are not well reproduced. The underdissociation of CH_4 appears to be the reason of the underestimation of H_2. The possible causes of the under-dissociation of CH_4 are investigated next in 5.2.

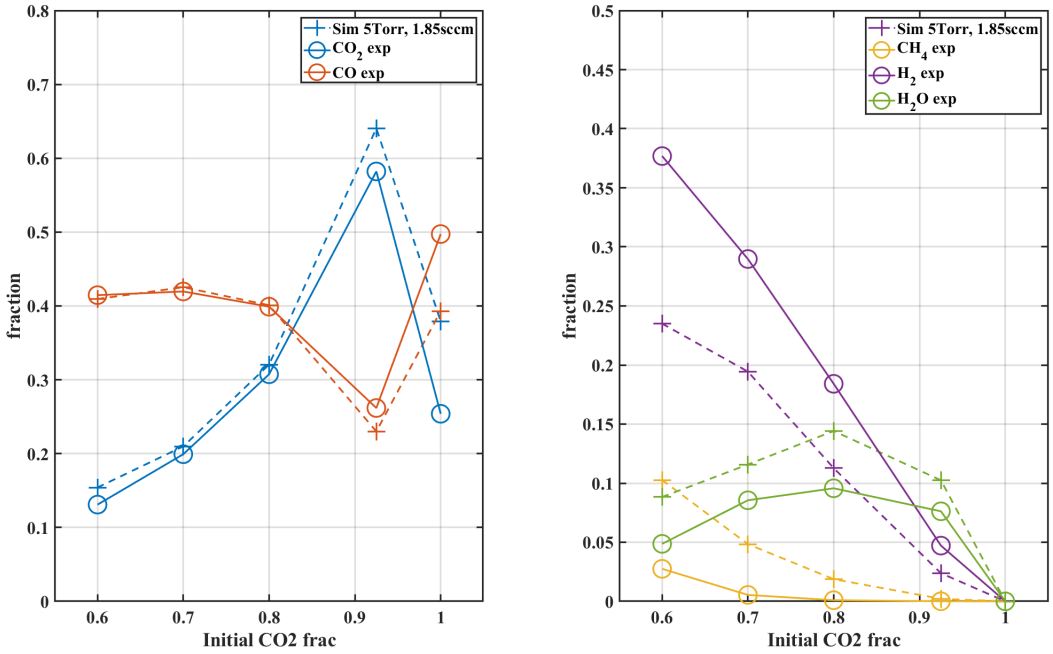

Figure 12: Comparison of the simulation and the experiment for a mixture variation at 1.85 sccm, 5 Torr. The simulation is plotted in dashed lines and the experiment in plain lines

5.2 Effect of CH_4 dissociation cross-section

As mentioned earlier, electron impact is one of the main dissociation process of CO_2 and CH_4 in our plasma. Because the simulated density of CH_4 is constantly overestimated, the hypothesis that the electron impact dissociation cross-section of CH_4 through the channels $e + CH_4 \rightarrow e + CH_3 + H$ and $e + CH_4 \rightarrow e + CH_2 + H_2$ could be underestimated arose. The dissociation cross-section for these two channels is taken from [44] where they are not measured directly but estimated from total dissociation cross-section and branching ratios. Though the cross-sections eventually chosen in [44] are the best fit for the validation against the swarm parameters, some experimental values of these cross-sections available in literature do show a factor of 2 compared to the one used in our range of interest ($\epsilon < 15$ eV) [55]. The CH_4 dissociation cross-sections were therefore kept as such for the computation of the EEDF (to keep a set of cross-sections validated against swarm parameters) but the corresponding dissociation rate coefficients were multiplied by a factor 2 when used in the chemistry part. This of course introduces an inconsistency between the Boltzmann solver and the chemistry solver but this has already been proved to be a good solution in some cases, for example to describe CO_2 dissociation [39]. The effect of this change on the calculation of the E/N, not shown here, is very minor. The effect of the doubling of CH_4 dissociation rate coefficient on the chemistry is shown on figure 13. The CO_2 and CO are only minorly modified by this change. The trends of the hydrogenated species are still reproduced for all conditions and the values are slightly improved by the doubling of the cross-section: the CH_4 percentage, previously at 11% in the 60:40 CO_2:CH_4 case, decreases to 9% (leaving still a factor ∼3 compared to the experimental value). In the same mixture, the H_2 goes from 23% without the doubling to 26% with, thus improving, while remaining far from the experimental 38% . Finally, still in the same mixture, the water density sees a minor improvement, going from 8.8% to 8%. The impact of doubling the CH_4 cross-section is therefore positive but still very limited. However, given the improvement and given that a factor 2 correspond to the upper values available in literature for CH_4 dissociation cross-sections, this change is kept in the model for the rest of this work.

5.3 Role of the O(^{1}D) state in limiting CH_4 back reaction

The previous subsection proved that the overestimation of CH_4 and underestimation of H_2 were not explained only by an underestimation of the CH_4 electron impact dissociation. The problem can therefore be taken the other way around: the back-reaction of H_2 could reform CH_4, lowering the H_2 density and increasing the CH_4 density. A back-reaction mechanism indeed exists and is taken into account in the model

$$H_2 + CH_3 \rightarrow CH_4 + H, \quad k = 2.52 \times 10^{-20} \times (\frac{T}{300})^{3.21} e^{-\frac{4380}{T}} m^3 s^{-1} \tag{12}$$

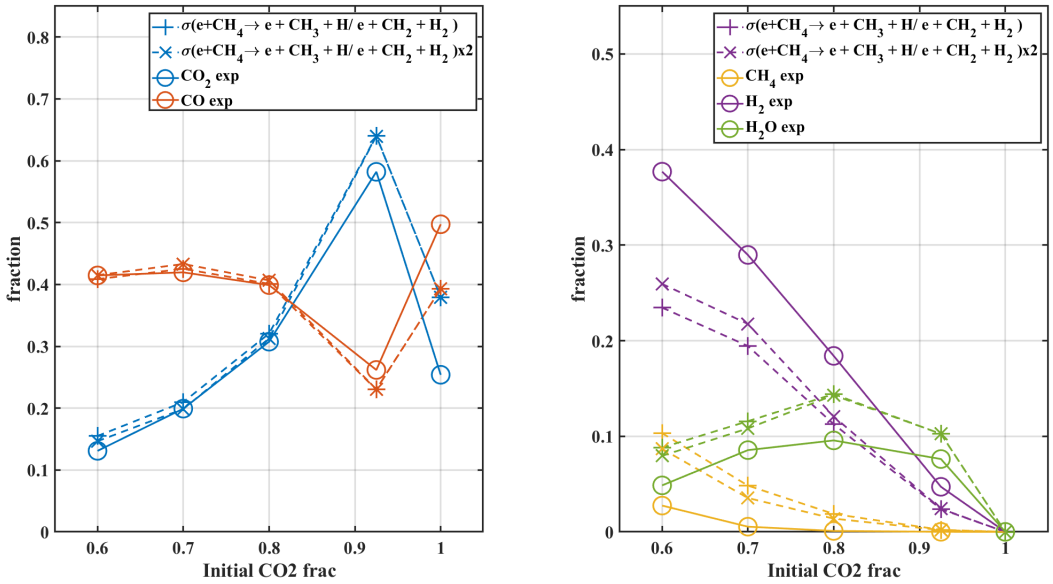

Figure 13: Study of the effect of the doubling of the CH_4 dissociation cross-section (taken from [44]) on the main products fractions at 1.85 sccm, 5 Torr. The experiment is plotted in plain lines, the simulation using the cross-section from [44] is plotted in dashed lines with + markers and the simulation with the cross-section doubled in dashed lines with x markers.

In the current reaction scheme, this reaction 12 is the main cause of formation of CH_4. The value of the rate coefficient is taken from [56] (given for the 300-2500K range), but other values given in [57] or [58] are of the same order of magnitude. All the other values for this reaction available on the NIST kinetic database are higher, sometimes by a factor 100. The 3 values quoted here are then at the bottom of the range of available rate coefficients. It is therefore unlikely that the back-reaction rate is overestimated. This could mean the reactants should be consumed in another reaction at a higher rate (presumably CH_3, because H_2 is underestimated in the model). The possibility of the reaction forming C_2H_6 from CH_3 ($CH_3 + CH_3 \rightarrow C_2H_6$) arises. However, the density of C_2H_6 that would have to be formed to obtain a good agreement on the CH_4 would add up to about 2.5% of the gas density, which would be detected with the FTIR measurement and this is not the case. Though the formation of C_2H_6 could contribute to a better agreement between model and experiment, it does not seem to be the mechanism involving CH_3 that would prevent the back reaction.
It was noted that the $O(^1D)$ excited state of atomic oxygen plays an important role in the plasma via reactions of $O(^1D)$ with CH_4, H_2 and H_2O (which are discussed in section 6). For example, the production of OH is partly due to

$$CH_4 + O(^1D) \rightarrow CH_3 + OH \tag{13}$$

The rate coefficients of these reactions are usually several orders of magnitude higher than the rate coefficients of the same processes with the $O(^3P)$ ground state (see table 4). We could not find in the literature any rate coefficient for the interaction of CH_3 with $O(^1D)$ and this reaction was not included in our kinetic scheme so far. As a test to assess the sensitivity of the results to a possible stronger oxidation of CH_3, one process was added to the kinetic scheme:

$$CH_3 + O(^1D) \rightarrow CO + H_2 + H \tag{14}$$

Its counterpart exists for the ground state $O(^3P)$. This process is very likely to occur in our plasma, because both CH_3 and $O(^1D)$ are direct dissociation fragments of the two input gases:

$$e + CH_4 \rightarrow e + CH_3 + H \tag{15}$$

$$e + CO_2 \rightarrow e + CO + O(^1D) \tag{16}$$

These two channels are the most probable dissociation channels for CO_2 and CH_4 in our plasma. Additionally, the transition $O(^1D) \rightarrow O(^3P)$ is forbidden, making the $O(^1D)$ a metastable species. The reaction (14) could therefore very well happen, but to the best of our knowledge, its rate is unknown. The next figure 14 shows the influence of process (14) on the chemistry with different values of the rate coefficient, varied between k_{14}=1 $\times$ 10^{-16} m^3s^{-1} and k_{14}=1$\times 10^{-13}$ m^3s^{-1}. The lower value k_{14}=1$\times 10^{-16}$ m^3s^{-1} is the order of magnitude of the same process with $O(^3P)$ at 600K. Because of the electronic energy of the $O(^1D)$ state ($\sim$ 1eV), the rate

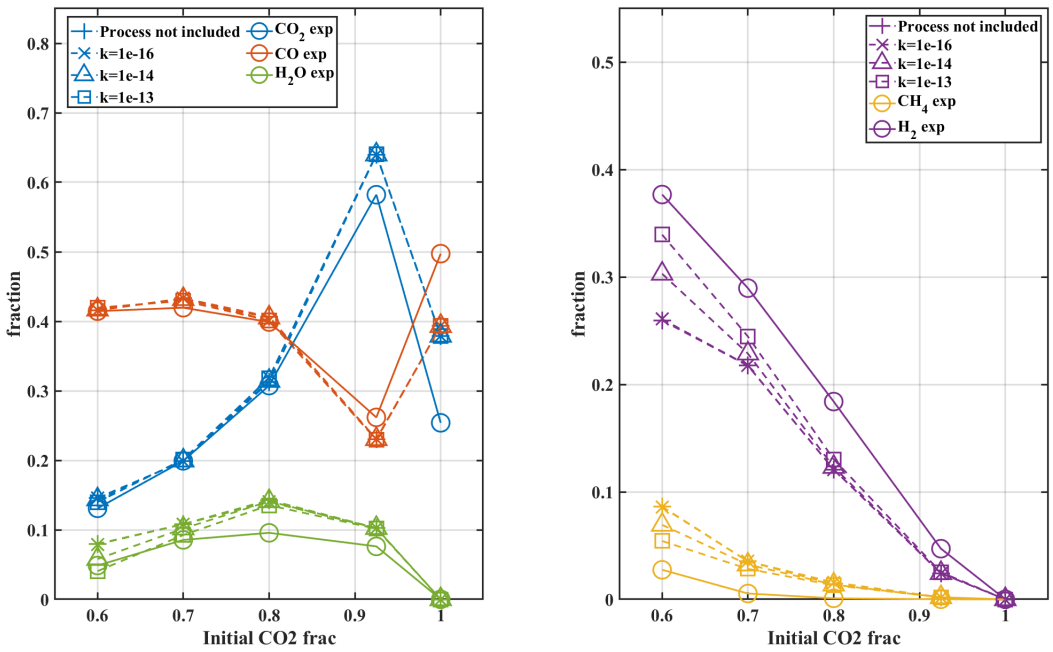

Figure 14: Study of the effect of the addition of process (14) on the main products fractions at 1.85 sccm, 5 Torr with different rate coefficient in m^3s^{-1}. The simulation is plotted in dashed lines and the experiment in plain lines

Process	Value with O(^{3}P)	at 300K	at 600k	value with O(^{1}D)
$CH_4 + O \rightarrow CH_3 + OH$	$2.26\times10^{-18}\times(\frac{T}{300})^{2.2}exp(\frac{-3819}{T})$	6.69×10^{-24}	1.79×10^{-20}	1.35×10^{-16}
$H_2 + O \rightarrow OH + H$	$3.4\times10^{-19}\times(\frac{T}{300})^{2.67}exp(\frac{-3159}{T})$	9.08×10^{-24}	1.12×10^{-20}	1.2×10^{-16}
$H_2O + O \rightarrow OH + OH$	$1.84\times10^{-17}\times(\frac{T}{300})^{0.95}exp(\frac{-8570}{T})$	7.25×10^{-30}	2.23×10^{-23}	2×10^{-16}

Table 4: Comparison of the rates coefficients (in m^3s^{-1}) of the reaction involving O(^{3}P) and O(^{1}D) available in literature. The source of the rates coefficients are available in supplementary information

coefficient k_{14} is expected to be higher than the one for O(^{3}P). The various simulations are plotted in dashed lines and the experiment is in plain lines. In this plot, due to the great number of curves overlapping, the water fraction was plotted with the CO and CO_2 fractions. First, the CO_2 and CO remain unchanged by this new process, and both trends and values are well reproduced. Looking at the CH_4 in yellow, the simulated fractions are significantly improved by the addition of the new process. In the case of the 60:40 CO_2:CH_4 mixture, a very minor difference is seen on the CH_4 fraction (of the order of 0.04%, from 8.63% to 8.59%) for k=1×10^{-16} m^3s^{-1}. In this same mixture, increasing k_{14} to 10^{-14} m^3s^{-1} decreases the CH_4 fraction to 6.9%. Finally, adding one extra orders of magnitude ($k_{14} = 10^{-13}$ m^3s^{-1}) bring the CH_4 fraction down to 5.4%. This value is still far from the 2.8% of CH_4 measured experimentally, but this process, depending on its rate, allows to greatly improve the predicted CH_4 fraction. The amelioration can be seen for all mixtures but with a lesser importance. Similarly, in a 60:40 CO_2:CH_4 mixture, the H_2 fraction is also increased with the rate of 14: the value without process 14 (26%) is raised to 30% with $k_{14} = 10^{-14}$ m^3s^{-1} and to 34% with $k_{14} = 10^{-13}$ m^3s^{-1}, not so far from the experimental 37%. The amelioration is also here seen for all percentages. Finally, looking at the water fraction at high CH_4 initial percentage (60:40 CO_2:CH_4), the simulated initial value (7.9%) is improved with $k_{14} = 10^{-14}$ m^3s^{-1} down to 5.7%, close to the experimental 4.8%. However when k is increased above 10^{-14}, the water fraction is underestimated, dropping below the experimental value (with 4% for $k_{14} = 10^{-13}$ m^3s^{-1}). The 60:40 mixture is the only case where this is observed; in all other mixtures, increasing k brings experiment and simulation closer. It therefore appears that a high value of the rate coefficient is largely beneficial for the agreement of CH_4 and H_2, and for the one of H_2O until a certain point, showing the interest of adding that process to the model. However, a reasonable value of the rate coefficient must be chosen. To this aim, the rate coefficients available in literature for reactions with O(^{1}D) and O(^{3}P) are compared in table 4. It appears that the rate coefficients of reactions involving O(^{1}D) can be 2 to 4 orders of magnitude larger than the rate coefficients of the same reaction involving O(^{3}P). In our conditions, the gas kinetic rate coefficient for O and CH_3 is of the order of 10^{-15} m^3s^{-1} and should be the upper limit of the rate coefficient. However, because the

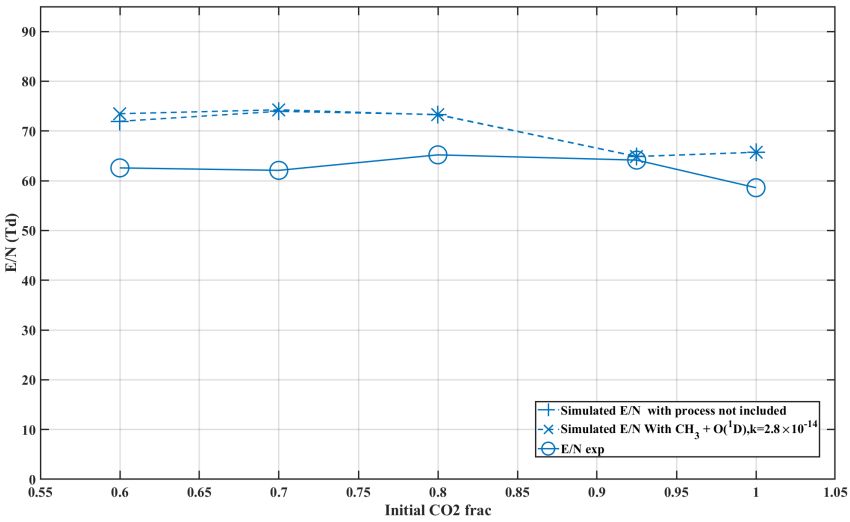

Figure 15: Comparison of the experimental and simulated reduced electric field (after inclusion of process 14 with the chosen rate coefficient) for an initial mixture variation at 1.85 sccm, 5 Torr. The experiment is in plain line and the simulation in dashed line

overall best agreement between modelling and experiment is obtained with a rate coefficient of 10^{-14} m^3s^{-1}, this value will be kept in the model despite being one order of magnitude higher than the gas kinetic rate. The high rate coefficient needed could suggest that the reaction (14) is an effective process, i.e a reaction grouping several processes. These other processes could involve other excited states like higher electronically excited O states or excited OH radicals. Process (14) is nevertheless kept in the model with the following rate:

$$CH_3 + O(^3P) \rightarrow CO + H_2 + H,\ k = 2.8{\times}10^{-17} m^3/s$$
$$CH_3 + O(^1D) \rightarrow CO + H_2 + H,\ k = 2.8{\times}10^{-14} m^3/s$$

This remains of course a rough approximation and further work is needed to determine the rate of this particular process and investigate the actual pathways of CH_3 destruction.

This illustration of the possible importance of the $O(^1D)$ state highlights the lack of data (even the absence!) for processes involving other electronically excited states. $O(^1D)$ is one of the very few excited states for which rate coefficients can be found for the interaction with hydrogenated species. No rate coefficient can be found for instance for the reaction $C_XH_Y + CO(a^3\Pi)\ \forall X\&Y$ despite the crucial role of $CO(a^3\Pi)$ in pure CO_2 plasmas put forward in [26]. The other excited states might also improve the model if properly taken into account.

It was verified that the addition of reaction (14) does not change the charge creation and the self-consistent E/N obtained in the simulations. The self-consistent reduced electric field at 1.85 sccm, 5 Torr is shown below on figure 15 along with the experimental reduced electric field. The agreement found earlier is maintained with the same gap: $|E/N_{sim} - E/N_{exp}|$ <12 Td. The trend with pressure must also be verified. The following figure 16 shows the comparison of the main species fraction and the reduced electric field for experiment and simulation. First, looking at the third graph of figure 16 (showing the reduced electric field), it appears that the addition of process (14) and the doubling of the CH_4 cross-section has only a minor impact on the electric field, which conserves a similar agreement as before. The divergence between experiment and simulation is still seen at low pressure. The 2 Torr measurement, which previously showed $|E/N_{sim} - E/N_{exp}|$ ~20 Td now shows a difference of 21 Td, showing the little impact overall. The fractions of CO_2 and CO, shown on the first graph of figure 16 are in very good agreement, both in trend and values. The CH_4 fraction is still overestimated by a factor slightly smaller than 2, but the trend is well reproduced and the gap only correspond to a few percent of the total gas density. The H_2 results are now in much better agreement. The maximum, previously shifted to 4 Torr in the simulation is now at the same pressure as the experimental maximum, though the simulated values are still a bit lower than the experiment.

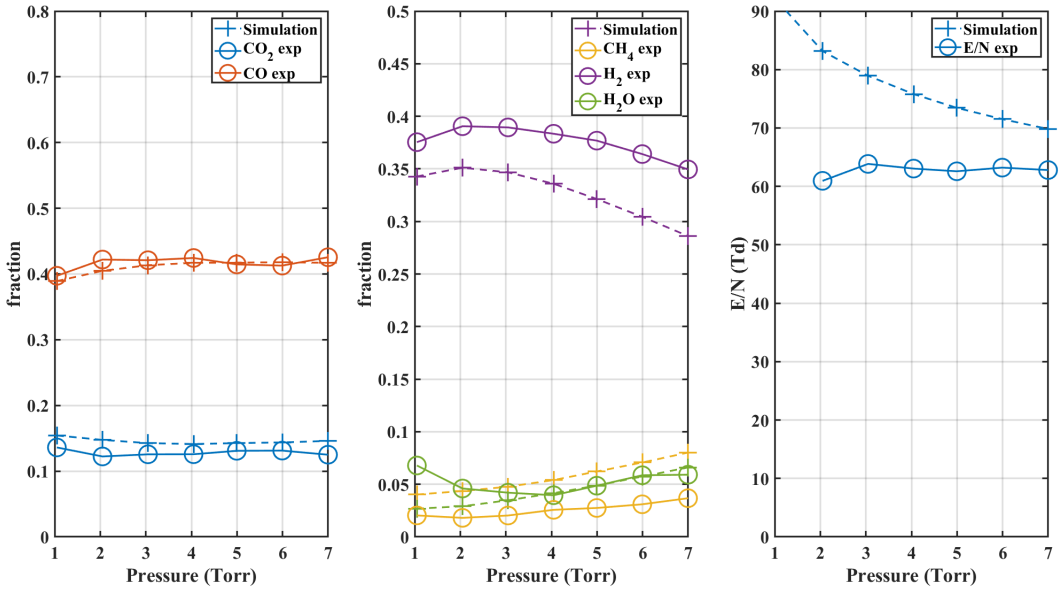

Figure 16: Comparison of experiment and simulation for the E/N and the main products densities (after inclusion of process14 with the chosen rate) for an pressure variation at 1.85 sccm in a 60:40 CO_2:CH_4 mixture. The experiment is in plain line and the simulation in dashed line

Reaction	Rate coefficient (m^3s^{-1})	Reference
$CH_4^+ + CH_4 \rightarrow CH_5^+ + CH_3$	1.5×10^{-15}	[59]
$CH_4^+ + H_2 \rightarrow CH_5^+ + H$	$4.89 \times 10^{-17} \times \frac{T}{300}^{-0.14} \times exp(-36.1/T)$	[59]

Table 5: CH_5^+ main creation mechanism

5.4 Effect of the CH_5^+ ion

In the model presented here, CH_4^+ is the main ion when the initial proportion of CH_4 is higher than 10%. It is usually found in literature that CH_5^+ is the main ion, as shown in the simulations from both [20] and [22], where it is the most abundant ion in two different types of discharge. The main reaction forming CH_5^+ in these discharges are listed in the table 5 with their rate coefficients and were not included in the model so far. The effect of their addition is discussed here. The rate coefficients are taken from the UMIST database (like in [20] and [22]). The effect of the two reactions on the simulation with the present kinetic scheme has been tested and is shown on figure 17. Only a minor impact is seen on the plasma chemistry, not shown here: the fractions are shifted by 1%, in the right direction for CH_4 and H_2 but in the wrong direction for CO_2 and CO. They have however a strong effect on both the reduced electric field and the ion densities, which are shown on figure 17. On the first graph of figure 17, the experimental reduced electric field is plotted in plain line and the simulated one is in dashed line. The case where the two reactions of table 5 are included is shown with x marker, the case without is plotted with + markers. A significant improvement is seen when the reactions are removed, with an improvement of about 8∼9 Td, reducing the gap between experiment and simulation to 11 Td in the 60:40 CO_2:CH_4 (vs 20 Td when the reactions are included). The reason of this improvement probably lies in the very high value of the rate coefficients of these CH_5^+ production reactions. The rate coefficients for these reaction are much larger than the typical rate coefficients of reactions forming the CH_5^+ ion ([60, 61]), leading to a change of the main ion when they are added to the model, as visible on the second graph on figure 17: when the reactions are added (with x markers), CH_5^+ (in red) is the main ion whereas it only accounts for 1% of the ion density when the reactions are not here (with + markers). The CH_4 is first ionized forming CH_4^+, followed by an efficient production of CH_5^+ (due to the high rate coefficient). However, CH_5^+ is much more easily destroyed than CH_4^+. First the reduced mobility of the CH_5^+ ion is about 1.5 times higher than the one of CH_4^+ ([62]), leading to higher diffusion and loss to the wall. Moreover, the main CH_5^+ recombination reaction is

$$e + CH_5^+ \rightarrow CH_4 + H \tag{17}$$

The rate coefficient of this reaction is one order of magnitude higher than the rate coefficient of any CH_4^+ recombination reaction. When the reactions of table 5 are included, charges are quickly transferred to CH_5^+ and lost. In turn, the reduced electric fields increases to ionize more CH_4 and compensate for the loss of CH_5^+.

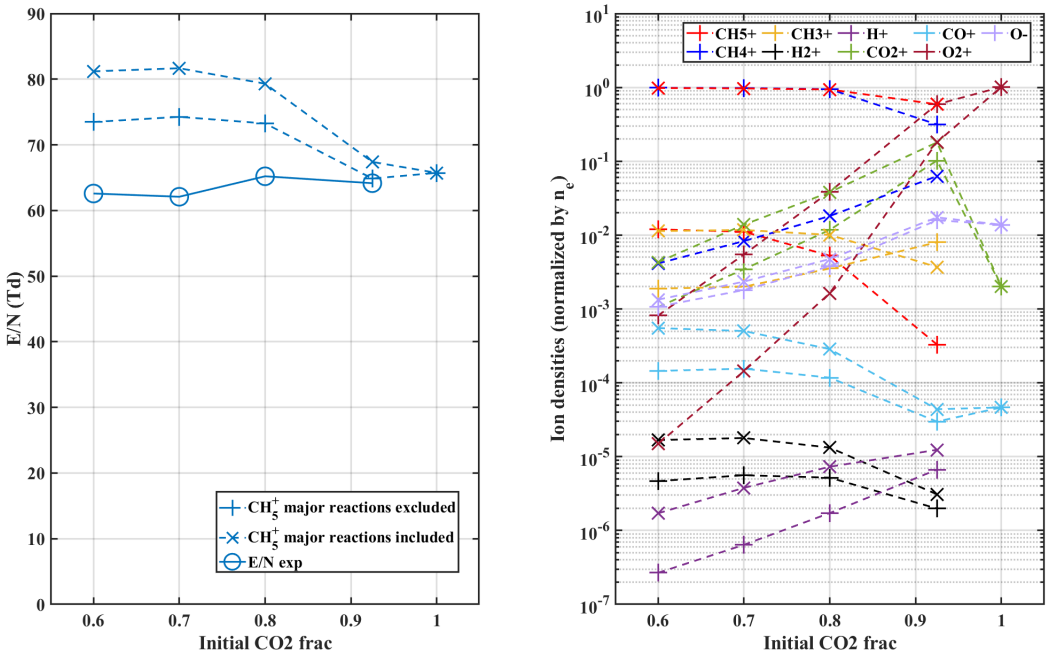

Figure 17: Effect of the CH_5^+ production reactions of table 5 on the electron kinetics in the case of a initial mixture variation at 1.85 sccm and 5 Torr. The case where the reactions are included are plotted with x markers, the case where they are not included are plotted with + markers

The improvement of E/N when the reactions of table 5 are removed points toward an overestimation of the rates of creation of CH_5^+. The rates used here were originally determined in [59] by mass spectrometry. Several other measurements are available in literature, like an experimental determination, again by mass spectrometry, from [63] which gives a rate coefficient of approximately 4×10^{-16} m^3s^{-1} for the first channel in our conditions (versus 1.5×10^{-15} m^3s^{-1} in [59]). In [64], the rate of reaction $CH_4^+ + CD_4$ was investigated by mass spectrometry between 80 an 300K and was found to be close to the value proposed by [59]. Because of the spread of the values and their impact on the reduced electric field and the dominant ion, it was decided not to include these reactions in the model. Though this choice has a limited impact on the plasma chemistry in our condition, it could be more important in other discharges where the ion have a stronger influence on the chemistry. For example, the reaction $CH_5^+ + C_2H_6 \rightarrow CH_4 + H_2 + C_2H_5^+$ accounts for approximately 10% of the CH_4 in the DBD of [20]. Further investigation is required to clear this particular point, such as measurements of the ion densities in the CO_2-CH_4 discharge by mass spectroscopy.

5.5 Effect of H recombination

The H atoms in the plasma play an important role in the overall kinetics. Along with CH_3, they are the main dissociation product of CH_4 and are therefore involved in many reactions. It is essential that they are correctly simulated. One of the main losses of H atom is the recombination of H into H_2 at the walls. As mentioned in section 4.4, the wall recombination of H atoms in the plasma is estimated based on literature measurements. The H atom recombination is expected to be faster than the O atom recombination, giving an indication of the minimum value expected for the H recombination probability. The real value however remains uncertain. A study of the influence of the recombination probability of H atoms at the wall, γ_H, is presented on figure 18 as a function of pressure in 60:40 CO_2:CH_4 mixture at 1.85 sccm. The influence of γ_H on the reduced electric field and main products fractions is presented for γ_H ranging from 10^{-4} (order of magnitude of the value chosen for O in pure CO_2 plasmas) to 10^{-1}. The influence on the reduced electric field is shown on the third plot of figure 18. The gap between experiment and simulation for E/N is increased with the value of the recombination probability. The difference between model and experiment however varies with pressure. The largest increase is seen at 4 Torr, where the value jumps from 71.5 Td for γ_H=10^{-4} to 76.5 Td for γ_H=0.1, farther from the experimental 63 Td. At other pressures, the increase in E/N is closer to 2∼3 Td, always increasing the difference between experiment and simulation. As for the chemistry, presented on the first two graphs of figure 18, the effect of the increasing γ_H is non monotonous and depends very much on the pressure. For H_2 between 2 and 7 Torr, using γ_H=10^{-2} always gives the highest H_2 density, with the best agreement

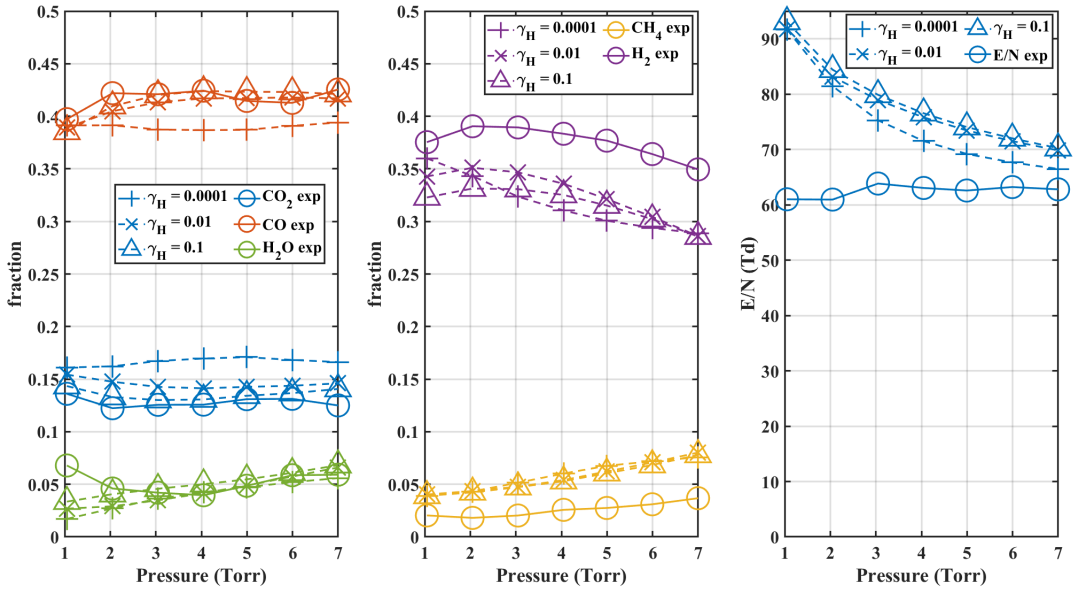

Figure 18: Study of the influence of the H wall recombination probability γ_H as a function of pressure in a 60:40 CO_2:CH_4 mixture at 1.85 sccm. The measurement are shown in plain line, the simulation is plotted in dash lines

with experimental H_2. The ordering of the H_2 densities obtained with γ_H=10^{-1} is not very clear and changes with pressure. This is probably due to a balance between electron impact dissociation processes producing atomic H and the back-reaction mechanism (12) ($CH_3 + H_2 \rightarrow CH_4 + H$). The increase of γ_H indeed increases the reduced electric field, in turn increasing electron impact dissociation of CH_4 and formation of atomic H through 15. H_2 formed by recombination of atomic H can react with CH_3 to reform CH_4. A balance of these processes probably explains the observed evolution of the H_2 density with γ_H. It must also be noted that the experimental trend of H_2 (with a maximum at 2 Torr) is only reproduced for $\gamma_H = 10^{-2}$ and $\gamma_H = 10^{-1}$. No clear trend can be established for the effect of the increase of γ_H, but it can be concluded that for all species showed here, the variation of γ_H over 4 orders of magnitude can change the fractions by $\pm$4%. The expected value of the recombination probability for Hydrogen is 10^{-3}, value proposed in [52] for low pressure hydrogen microwave discharge, or 10^{-2}, 10 to 100 times higher than O from values drawn from [32] for O. γ_H=10^{-2}, which allows capturing the maximum of H_2 at 2 Torr, is kept for the rest of this work. It must also be well noted that the wall recombination probability is expected to vary with pressure, as shown for O atoms in [32] where the γ_O, the recombination probability of atomic O in a O_2 plasma can vary by a factor 4.5 between 2 and 5 Torr. Keeping a constant value of γ_H with pressure is an approximation, which should be refined in further work.

5.6 Effect of the flow

So far, only the pressure and gas mixture variation have been investigated. The validity of the model for different flows must also be tested. The effect of the flow variation is shown on figure 19, where the flow is varied from 1.85 to 7.4 sccm at 5 Torr in a 60:40 CO_2:CH_4 mixture. Decreasing the flow increases the residence time of the gas in the plasma and therefore increases the energy input in the gas via electron impact reactions. It is therefore expected that decreasing the flow increases the dissociation for both CO_2 and CH_4. This is observed on figure 19, where the fractions of CO_2 and CO show an almost linear trend with the flow. The evolution of the main hydrogenated species CH_4, H_2 and H_2O in the simulation generally reproduce the trends observed experimentally for all gas flows. The simulated values show however the same overestimation of CH_4 and underestimation of H_2O as discussed before (up to a factor 2 for the CH_4 at low flow, as presented in the previous section). The lower flows emphasize more the role of the chemistry because the proportion of gas being renewed by incoming flow is lower. The rest of the discussion will therefore focus on the case with a total flow of 1.85 sccm only.

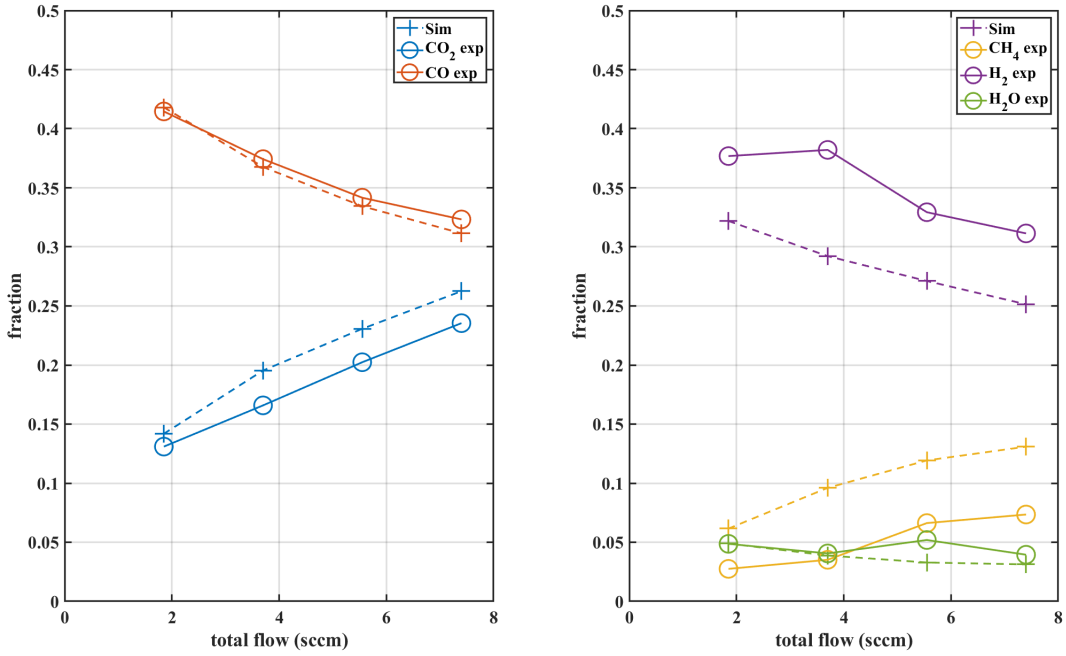

Figure 19: Comparison of the simulated and experimental fractions of the main species as a function of the flow for a 60:40 CO_2:CH_4 mixture at 5 Torr

5.7 Conclusions on the presented model

Overall, the model provides a good agreement between experiment and simulation for the whole range of parameters explored (pressure from 1 to 7 Torr, from pure CO_2 to 60:40 CO_2:CH_4 and for flows going from 7.4 sccm to 1.85 sccm). The main trends of the evolution of the densities of the different species with these parameters are correctly described, while the quantitative agreement remains always within a factor 2. The simulated points at low pressure show a discrepancy in the reduced electric field, indicating that the charges creation and loss processes are not all well accounted for at low pressure, likely because of the diffusion scheme of the ions used (see section 5.1). Other diffusion schemes tested could however not improve these results. Therefore, the insights from the model on the behaviour of the plasma at low pressure (1 Torr or below) should be taken with caution.

The results suggest that the electronically excited state $O(^1D)$ plays an important role in the kinetics of hydrogenated species. In fact, although some discrepancies remain, the addition of process (14) of oxidation of CH_3 by $O(^1D)$ significantly improves the agreement between experiment and simulation on the concentrations of these species. This finding may affect the influence ascribed to C_2H_Y molecules on the overall chemistry by models including only a simplified kinetics of $O(^1D)$ that misses reaction (14) or simply do not consider this species [22, 20]. In particular, if the electronic states are properly described, the role of C_2H_Y molecules might be much less prominent than often predicted. Note, however, that in our experiments C_2H_4 is detected at high flow, *i.e.*, low residence time, pointing towards a role of this species as an intermediate to further chemistry. Evidently, it is expected that when operating at higher pressure $O(^1D)$ is quenched by collision very quickly (which also happens here, see section 6) and its density is lower than in the present conditions. Nevertheless, it is still important to take it into account in the models, due to its much stronger reactivity than $O(^3P)$ in many reactions. Moreover, it has been shown that when computing the gas temperature self-consistently the conversion of electronic excitation to translational energy must be taken into account [65]. To clearly determine the relative role of $O(^1D)$ and the one of large molecules, future work may focus on the improvement of the kinetic scheme by including the chemistry of C_2H_Y molecules

6 Discussion of the reaction pathways

Now that the validity of the model has been verified by comparison with the experiment, it is used to understand more in details the processes of formation of the main species, as well as the role of the minor and/or unmeasured species such as the OH radicals, the CH_2O or the excited state $O(^1D)$, whose role was highlighted in the previous section. This discussion will also be useful in understanding some of the results

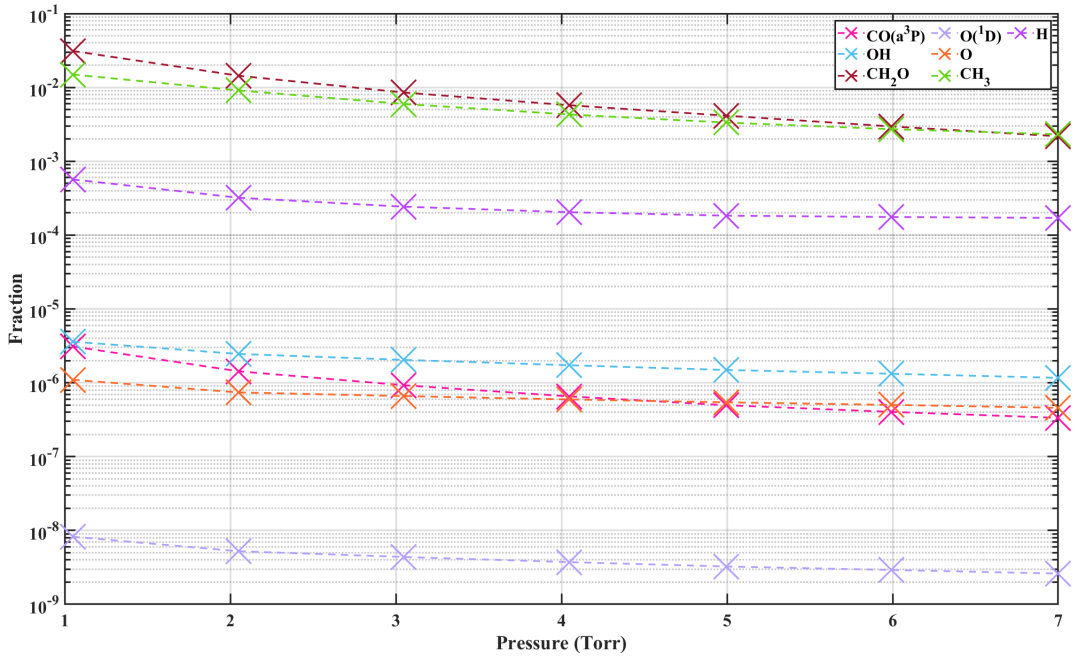

Figure 20: Evolution of the simulated fractions of minor species with pressure in a 60:40 CO_2:CH_4 mixture at 1.85 sccm.

observed on CeO_2 exposed to the same plasma in Part II of this article [27]. The mechanisms driving the chemical paths depend on the parameters varied (pressure and gas mixture), therefore the influence of each parameter is discussed separately.

6.1 Effect of pressure on CO_2-CH_4 plasmas main products

Varying the pressure in our glow discharge changes mostly the gas temperature from 300 K to ~700K at 7 Torr. As seen previously, the reduced electric field remains stable with pressure when the initial CH_4 percentage is above 10%. For most of the major species, the densities evolve in a limited range with pressure, as visible on figure 16. For all pressures, CO_2, H_2O and CH_4 remain respectively around 12, 5 and 7%, while CO evolves in a larger yet still narrow range between 36 and 44% of the total plasma density. The experimental variation of H_2 is also restrained in the range 35-40% of the plasma density. This limited evolution with a strongly increasing temperature (from 400K to 700K) proves already that the thermal dissociation of CH_4, which starts above 500K [9], is not a major contribution in the dissociation observed here. This illustrates the interest of cold plasmas to achieve DRM.

Before discussing the reaction pathways explaining the major species densities, the fractions of minor species which are often the most reactive ones must be known. The figure 20 shows the evolution of the minor species with pressure in a 60:40 CO_2-CH_4 mixture at 1.85 sccm computed by the model. The plot includes atomic O and H, the formaldehyde (CH_2O), the excited state O(^{1}D) (whose role was highlighted above), and the radicals OH and CH_3. For clarity, the other CH radicals (CH_2, CH and C) were not plotted due to low densities but are computed in the model.

Unlike the major species, the fractions of the minor species are all decaying with pressure. CH_2O varies by an order of magnitude between 2 and 7 Torr (from 1.4% at 2 Torr to 0.2% at 7 Torr), like CH_3. This is similar to [20] where the CH_2O was also the highest 'minor species', representing ~0.1% of the density. In [20] where conditions with up to 30% of initial CH_4 where modelled, the CH_2O density was close to the CH_3OH density, not included in the present model. These values seem however to be overestimated. The CH_2O is an IR active molecule and can therefore be detected with the FTIR with a sensitivity limit of 10^{20} m^{-3} in our experimental setup, which corresponds to approximately 0.3% of the mixture at 2Torr. The values predicted by the model at pressure should therefore be observed by the FTIR, which is not the case. It can be assumed that the values predicted by the model are overestimated by at least a factor 4 at 2Torr. The formation mechanisms of CH_2O are discussed further in section 6.2 to identify the origin of this discrepancy. The least varying species is the OH, decreasing only by a factor 3 from 1 to 7 Torr. The decrease of the radical density with pressure is expected due

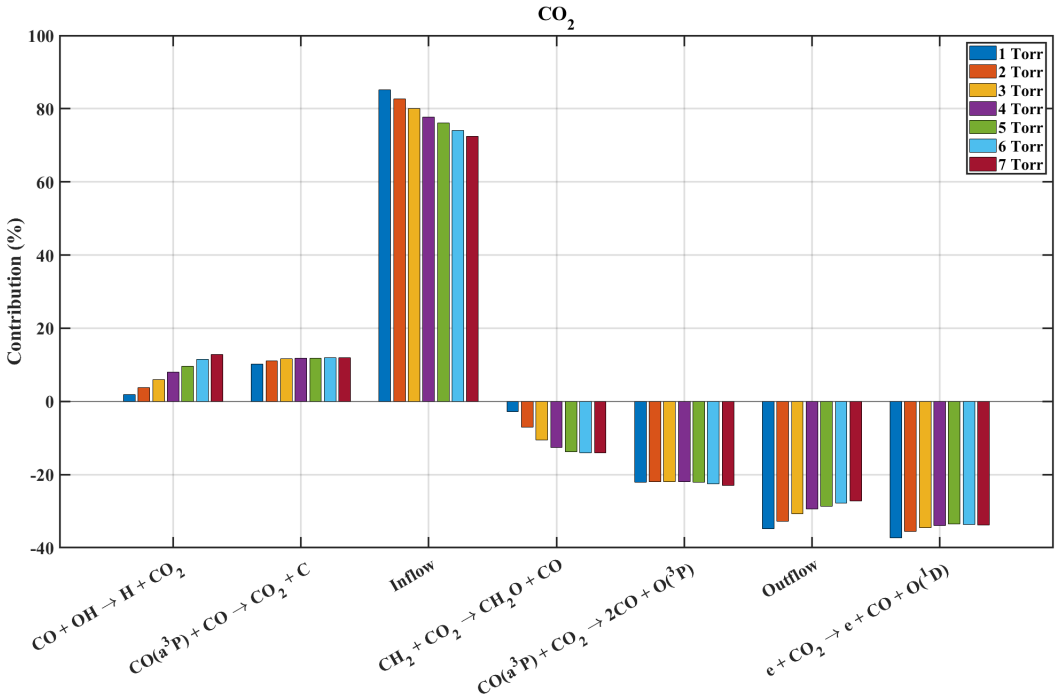

Figure 21: Evolution with pressure of the contribution of the main creation and destruction channels of CO_2 in a 60:40 CO_2:CH_4 plasma at 1.85 sccm. The positive contribution represent the creation, the negative the destruction processes. Each pressure is plotted in a different color

to both the increase of the gas temperature (which increases the rate coefficients of recombination reactions) and the increasing collision frequency (and therefore recombination reactions) with pressure. The simulated O fraction is about 1×10^{-6}. This is very low but possible as O is below our actinometry detection level in the 60:40 CO_2:CH_4 condition studied here. The H fraction varies between 0.05 and 0.01%, one order of magnitude lower than actinometry estimation, which could be due to the wall recombination probability (whose order of magnitude is unknown).

The aim of this section is to understand the evolution of the main processes driving conversion in CO_2-CH_4 plasmas as a function of the pressure.

Creation and loss processes of CO_2

The evolution of the processes creating and destroying CO_2 with pressure is shown on figure 21 in a 60:40 CO_2:CH_4 plasma at 1.85 sccm. The processes are represented in a form of a bar graph, with the contribution of each process (in %) at steady state. The positive contributions represent the creation, the negative the destruction processes. Each pressure is plotted in a different color. In this condition (60:40 CO_2:CH_4 at 1.85 sccm), CO_2 is destroyed through 3 main channels independently of pressure: the outflow accounts for about as much as the electron impact dissociation forming CO and $O(^1D)$ (reaction 16). The third important destruction channel of CO_2 involves $CO(a^3\Pi)$ as described in [26] and [66]:

$$CO(a^3\Pi) + CO_2 \rightarrow 2CO + O(^3P) \tag{18}$$

The main source of CO_2 is the inflow, showing that the state reached in the reactor is only a pseudo-steady state where the dissociation is compensated by the renewal of the gas. The creation of CO_2 is also steadily assured by recombination of $CO(a^3\Pi)$ through:

$$CO(a^3\Pi) + CO \rightarrow CO_2 + C \tag{19}$$

This process is critical in pure CO_2 (as shown in [26] or in [66]) and seems to play here an important role as well but is usually not mentioned in other CO_2-CH_4 plasma models from literature. In pure CO_2 plasmas, the $CO(a^3\Pi)$ also strongly contributes to the reformation of CO_2 with the back-reaction

$$CO(a^3\Pi) + O_2 \rightarrow CO_2 + O \tag{20}$$

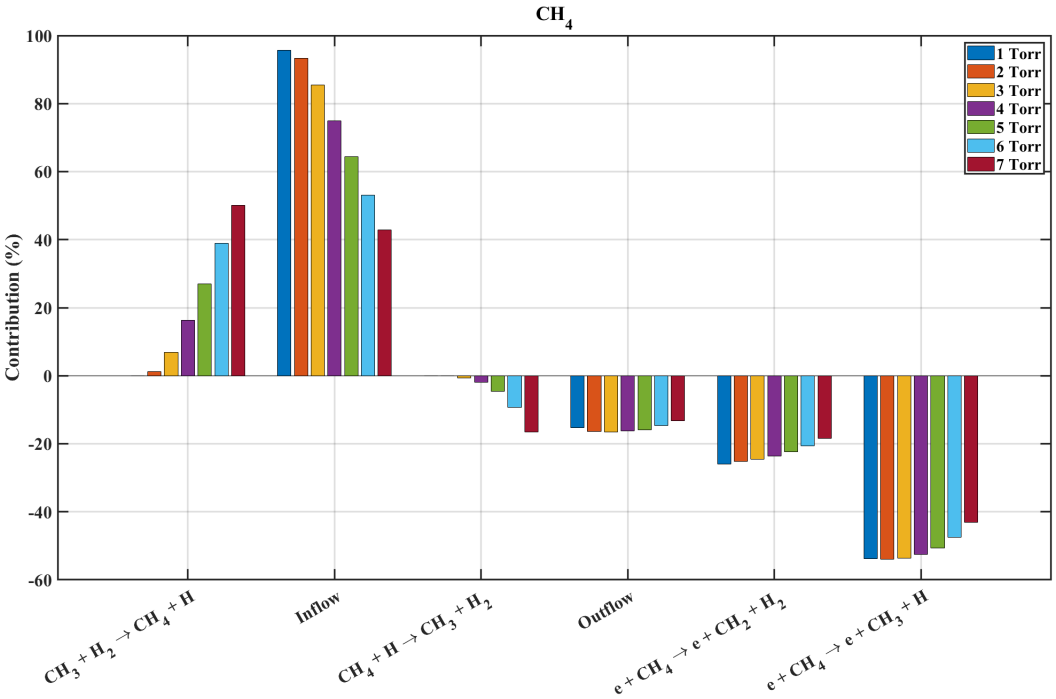

Figure 22: Evolution with pressure of the contribution of the main creation and destruction of CH_4 in a 60:40 CO_2:CH_4 plasma at 1.85 sccm. The positive contribution represent the creation, the negative the destruction processes. Each pressure is plotted in a different color

This reaction is negligible in the 60:40 CO_2:CH_4 plasma because of the very low density of O_2. However, the interaction of CO($a^3\Pi$) is in this work only taken into account with CO_2 and CO and O_2. This once again points toward the importance of excited species and the necessity to obtain rate coefficients s in particular for reactions of $CO(a^3\Pi)$ with hydrogenated species which to the best of our knowledge are not reported. With rising pressure, the contribution of the back-reaction :

$$CO + OH \rightarrow CO_2 + H \tag{21}$$

largely increases with pressure. This back-reaction mechanism (representing approximately 10% of CO_2 creation) was identified in [20] in a DBD with a contribution of 9%, close to the one computed here. The reaction was not identified in nanosecond discharges in [22], but [25] (also in NRP) claimed that the inverse process (CO_2+H) helped the dissociation. However, the model in [25] does not focus on the reaction pathways (no reaction rate is given) and process (21) is just a lead to explain the results. In [67], where DRM is studied in a gliding arc plasmatron, the inverse process (CO_2+H → CO + OH) is the main dissociation process of CO_2. Similar results for a gliding arc were found in [68], where up to 90% of the dissociation was attributed to CO_2+H at high initial CH_4 content. This could be due to the higher temperature in the GA (>2500K) compared to the glow (<1000K). The comparison of the rate coefficient of CO+OH (taken from [69] in our work) with the rate coefficient of CO_2 +H (taken from [56] in our work) shows that the first one is several orders of magnitude higher than the second at temperatures below 1000K, but that the rate coefficient of CO_2 + H becomes higher than the one of CO+OH at temperature above 2400K. This explains why the reaction reforms CO_2 in our discharge but dissociates it in the GA. Despite the numerous processes at play, the destruction and production of CO_2 are relatively constant for all pressures studied.

Creation and loss processes of CH_4

The destruction of CH_4 is also quite stable with pressure as visible on figure 22.

For all pressures, CH_4 at pseudo-steady state is lost mostly through outflow and electron impact dissociation:

$$e + CH_4 \rightarrow e + CH_3 + H \tag{15}$$
$$e + CH_4 \rightarrow e + CH_2 + H_2 \tag{22}$$

with the first one being twice as important as the second one. CO_2 main loss was the outflow, before electron impact dissociation but it is the opposite for CH_4, for which electron impact dissociation is dominant, with

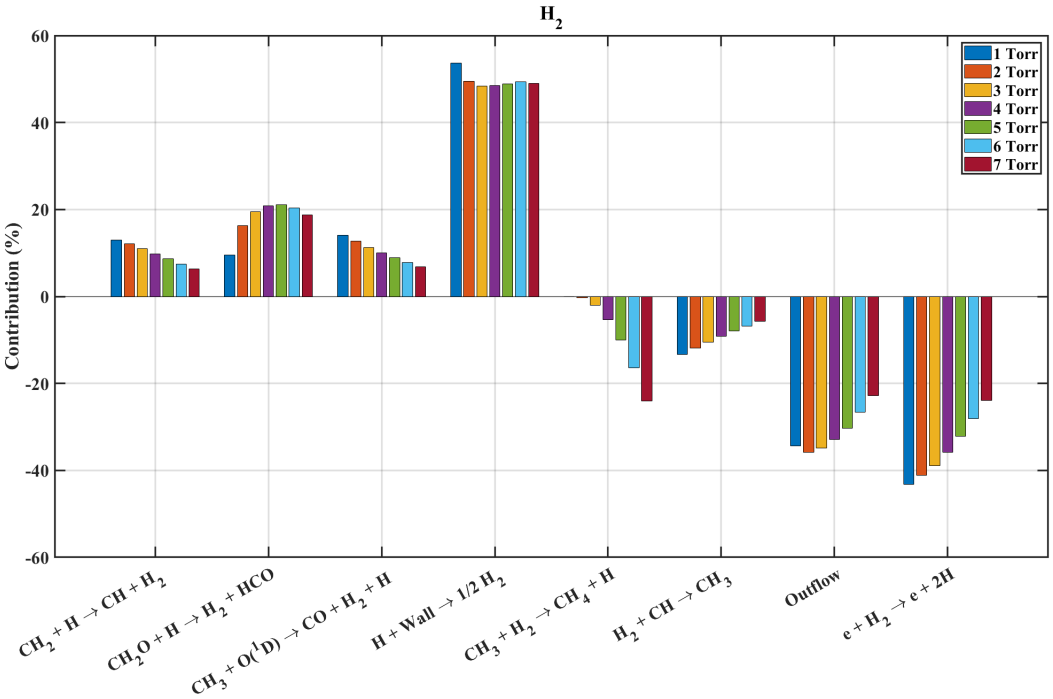

Figure 23: Evolution with pressure of the contribution of the main creation and destruction of H_2 in a 60:40 CO_2:CH_4 plasma at 1.85 sccm. The positive contribution represent the creation, the negative the destruction processes. Each pressure is plotted in a different color

approximately 60 to 70% of CH_4 lost by electron impact. The two species have very close dissociation thresholds (around 7.5eV) and the difference is therefore explained by the greater amplitude of the CH_4 dissociation cross-section. In [20], the electron impact yielding CH_3 and H (process 15) contributes to 33% of CH_4 destruction (not too far from the 40-50% simulated in our conditions) whereas the channel yielding CH_2 accounts for only 6% (a factor 4 lower, compared to a factor 2 for us). This likely comes from the CH_4 dissociation cross-section: [70] was used in [20] whereas [44] was chosen in our case. As discussed in section 5.2, the more recent source [44], is a set of cross-sections validated against the swarm parameters and based on experimental measurements. The cross-sections proposed in [70] is based on calculations and analytical fitting of experimental ionization cross-sections. Both sources yield different branching for CH_4 cross-section. The cross-sections from [44] were chosen but the chemistry with the branching ratio proposed in [70] should also be tested in future work. Dissociation of CH_4 by electron impact was also the main dissociation process in the ns discharges of [22], as expected with the very high electric field of the nanosecond discharge. The loss of CH_4 via ion recombination is very weak in our model, as opposed to [20], where 18% of the loss of CH_4 is attributed to the production of CH_5^+: $CH_4^+ + CH_4 \rightarrow CH_3 + CH_5^+$. This reaction is very weak in our work due to the low production of CH_5^+ as discussed in section 5.4. A last main loss process of CH_4 is the direct reaction:

$$CH_4 + H \rightleftharpoons CH_3 + H_2 \tag{23}$$

However, the contribution to CH_4 formation by the inverse reaction is higher. Overall the net balance of these two processes lead to formation of CH_4. The contribution of this process (12) strongly increases with pressure, becoming the dominant CH_4 creation channel at 7 Torr. This could change with the value of the H atoms recombination probability γ_H chosen. The other creation channel of CH_4 in our plasma, is the inflow. In [20] (a plug flow configuration as well), 30% of CH_4 production is attributed to electron impact dissociation of C_3H_8, 27% to dissociation of C_3H_6 and 16% to dissociation of C_2H_6, underlining the importance that these species can have if the plasma description relies on C_XH_Y.

Creation and loss processes of H_2

The processes forming and destroying H_2 vary significantly with pressure, as shown on figure 23. One thing draw the attention: at all pressures, almost 50% of H_2 is produced by wall recombination, which is understandably not described in the other CO_2-CH_4 plasma models available that are describing plasmas at atmospheric pressure. In our condition the contribution of the wall to H_2 production decreases when the pressure increases (like for O atoms recombination at similar pressures in [32]). In the 60:40 CO_2:CH_4 mixture shown on figure 23,

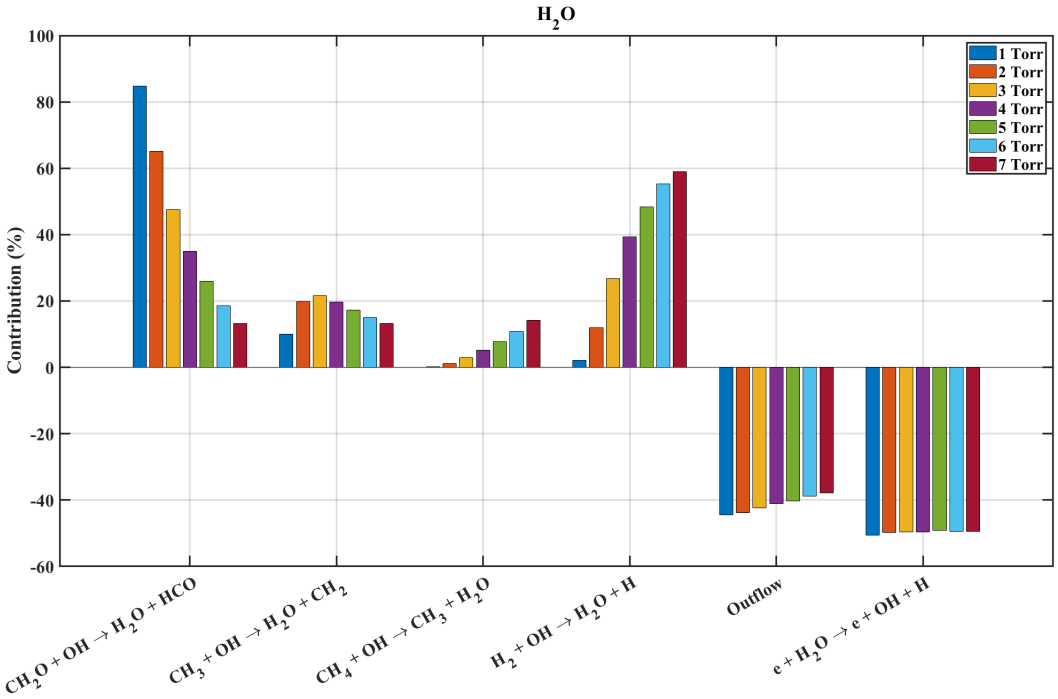

Figure 24: Evolution with pressure of the contribution of the main creation and destruction processes of H_2O in a 60:40 CO_2:CH_4 plasma at 1.85 sccm. The positive contribution represent the creation, the negative the destruction processes. Each pressure is plotted in a different color

the other H_2 formation channels are of course the process (14) (discussed in depth before), and 2 recombination channels of H with CH_2 or CH_2O. These 3 channels each account for 10 to 20% of the formed H_2. In [20], H_2 formation is attributed to electron impact of C_2H_Y and C_3H_Y molecules, totaling 60% of the H_2 production and highlighting the role attributed to large C_2H_Y molecules. This points once again toward the uncertain role of these large molecules in the kinetic scheme. In [22], H_2 formation is mostly attributed to CH_4 electron impact dissociation. This difference could find its root in the very high electric field applied in the NRP. With such an electric field, the electron impact dissociation would be greatly enhanced, explaining the importance of this channel. For all pressures, the outflow and the electron impact dissociation of H_2 are the major channels in the 60:40 CO_2:CH_4 mixture. In [20], a plug flow configuration, the in- and outflows are not taken into account and the electron impact dissociation is responsible for 90% of the H_2 loss. In our case, it is responsible for only half of the losses. However, if we do not include the outflow, electron impact of H_2 is indeed 90% of the losses. At high pressure, the back-reaction to CH_4 becomes as important as the two other destruction channels. Destruction channels of H_2 are not mentioned in [22].

Creation and loss processes of H_2O

The evolution with pressure of the creation and loss processes of water are presented on figure 24. The creation of H_2O is far from being constant with pressure: the most important process at 1 Torr ($CH_2O + OH \rightarrow H_2O + HCO$) is completely negligible at 7 Torr (following the evolution of CH_2O which is lowest at 7 Torr). At 7 Torr, $H_2 + OH \rightarrow H_2O + H$ is the main process. It is interesting to note that all the processes leading to formation of water involve OH. The water losses in the 60:40 CO_2:CH_4 plasma are however very steady with pressure: electron impact accounts for half of the loss, while the other half is carried away by the outflow. The electron impact dissociation leads to OH formation, thus establishing an equilibrium between OH and H_2O in the steady state. Because water is not identified as an important product in the other models, its main production or loss processes are usually not described. In [20], the measurements supporting the model seem to indicate that the water fraction is close to 1×10^{-4}, far from our 10%. This could be linked to the high pressure, which will efficiently quench the excited state necessary to form water (see next section).

Varying the pressure do not affect strongly the fractions of all the main species, despite the fact that some reactive minor species are varying with pressure. The fraction of minor species tend to decrease with pressure as expected with faster recombination/reactivity at higher collision frequency. The fractions of major species are relatively stable in the explored range of pressures (1-7 Torr). In our conditions the balance of the main species

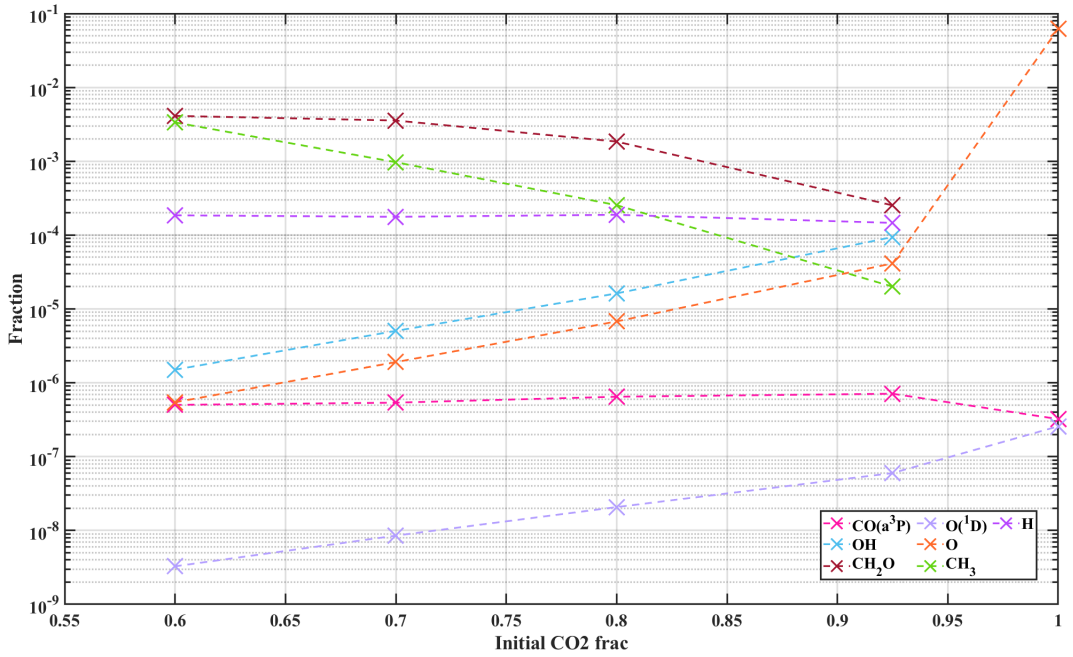

Figure 25: Evolution of the simulated fractions of minor species with initial CO_2:CH_4 ratio at 1.85 sccm and 5 Torr.

is controlled only by a few processes which could help future efforts of kinetic scheme reduction, but the role of electronically excited states (in particular CO($a^3\Pi$) and O(^{1}D)) should probably be more studied. In the part II of this paper [27], the species forming at the surface of CeO_2 exposed to the same plasma as described here will be studied. Formaldehyde (CH_2O) as well as water (and OH radicals) will be shown to have an important role on the surface kinetics on CeO_2. The strong change observed here for these species between 1 and 5 Torr (CH_2O fraction decreases almost by a factor 10 in this range of pressure) will be a valuable information for the understanding of the surface mechanisms in part II.

Knowing that the dominant processes remain the same with pressure, the effect of the CH_4 percentage in the initial mixture is studied at 5 Torr in the next section.

6.2 Effect of the initial mixture

As expected, varying the gas mixture from pure CO_2 plasma to a 60:40 CO_2:CH_4 plasma has a strong influence on the chemistry induced. In pure CO_2 plasmas, the main species are CO_2, CO, O_2 and atomic O. When a small fraction of CH_4 is introduced in the gas mixture, H_2, CH_4 and H_2O start appearing at levels higher than O_2 and O.

The evolution of the simulated fractions of minor species with the initial CH_4 content are shown on figure 25. The CH_3 and CH_2O fractions increase with admixture of CH_4 in the initial mixture as expected. The H atoms remain stable with the increase of initial CH_4 content because the loss of H is dominated by the very strong H recombination at the wall. The density of atomic H is then controlled by the diffusion of H to the walls. The OH density decreases with admixture of CH_4. However, surprisingly the peak of H_2O is reached at 80:20 despite the fact that OH and H_2O are related through several processes as seen in previous section. It can be noticed that OH and O densities have similar behaviours, both decreasing with increasing initial CH_4 content. The decrease of the O density matches the experimental actinometry results. The O(^{1}D) decreases with the increasing CH_4 similarly to O atoms, due to both the decreasing fraction of CO_2 and to the high rate coefficient chosen for reaction (14). Finally, the CO($a^3\Pi$) slightly increases when going from pure CO_2 to low initial CH_4 content. The CO($a^3\Pi$) density remains stable upon further admixture of initial (7×10^{-5}% in the 92:8 CO_2:CH_4 condition, 5.5×10^{-5}% at 60:40 CO_2:CH_4. The increase of the CO($a^3\Pi$) density when going from pure CO_2 to 95:5 CO_2:CH_4 is likely due to the drop of the O atoms density that are the main quenchers of CO($a^3\Pi$).

Because the densities of the main species are not monotonous with the increase of the initial CH_4 content (deep in CO_2 conversion at CH_4 percentage, peak in water fraction...), the processes controlling the plasma

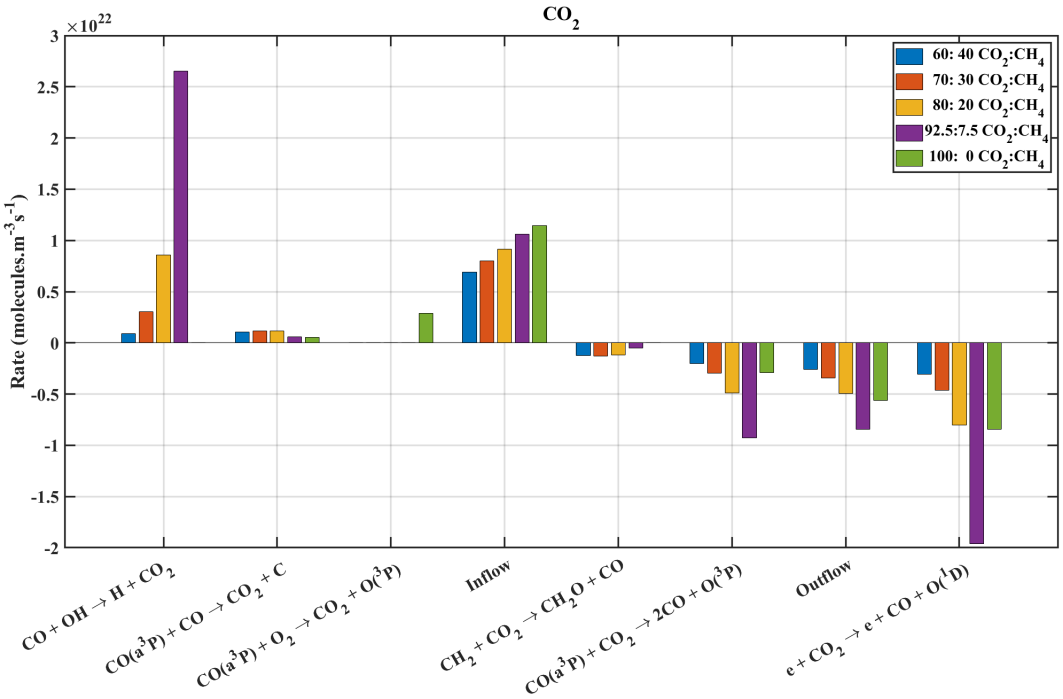

Figure 26: Evolution with initial mixture of the reaction rates of the main creation and destruction processes of CO_2 at pseudo-steady state at 1.85 sccm, 5 Torr. The positive rates represent the creation, the negative the destruction processes. Each initial mixture is plotted in a different color.

composition are expected to be quite different at low or high initial CH_4. One of the most noticeable behaviours is the peak in CO_2 fraction observed on figure 4 in the 95:5 CO_2:CH_4 mixtures for all pressures and all flows. To shed light on the processes driving CO_2 dissociation as a function of the initial CH_4, the rates of the main CO_2 loss and creation processes are plotted on figure 26. Each initial mixture is plotted with a different color. The positive reaction rates represent creation processes, the negative are loss processes. One difference is to note with the previous section (for pressure variation): while the contribution in % was plotted in the previous section because the rates scale with pressure, it is now the rates that are plotted because the pressure is kept constant at 5 Torr. The rates are plotted for a total flow of 1.85 sccm.

For each process (each x-axis tick), the rate of the process in the 60:40 mixture is plotted first on the left, followed by the 70:30, 80:20, 92:8 and finally the 100:0 mixtures.

Creation and loss processes of CO_2

Mainly four processes destroy CO_2, independently of the initial gas mixture. The three main ones (electron impact on CO_2 16, outflow and dissociation by $CO(a^3\Pi)$ 20). The rates of these 3 processes follow the evolution of the CO_2 density (which peaks in the 92:8 mixture). The fourth process is

$$CH_2 + CO_2 \rightarrow CH_2O + CO \tag{24}$$

The rate of process (24) increases with the initial amount of CH_4 because the limiting reactant in this process is the CH_2, a direct dissociation product of CH_4.
The rate of dissociation by $CO(a^3\Pi)$ (process 18) can be compared to the rate of creation of CO_2 by $CO(a^3\Pi)$ (process 20). The process (20), negligible for most conditions, accounts for 10% of the CO_2 production at 60:40 CO_2:CH_4. In this condition, $CO(a^3\Pi)$ dissociates twice as much CO_2 as it produces it (the reaction rate of (20) is 1×10^{21} $cm^{-3}s^{-1}$ versus 2×10^{21} $cm^{-3}s^{-1}$ for (18) at 60:40). In the other gas mixtures, the rate of (18) is always higher than the one of (20), meaning that in all the mixture $CO(a^3\Pi)$ is beneficial for CO_2 dissociation. Two processes stand out for the formation of CO_2: the inflow and the back-reaction (21) previously identified. The latter shows a very strong rate in the 92:8 mixture and is the main source of formation of CO_2 in this condition. This means that the back-reaction (21) ($CO + OH \rightarrow CO_2 + H$) is responsible for the peak in CO_2 fraction observed in this condition on figure 4, which is consistent with the OH density being maximum in the 92:8 CO_2:CH_4 condition.

Creation and loss processes of CH_4

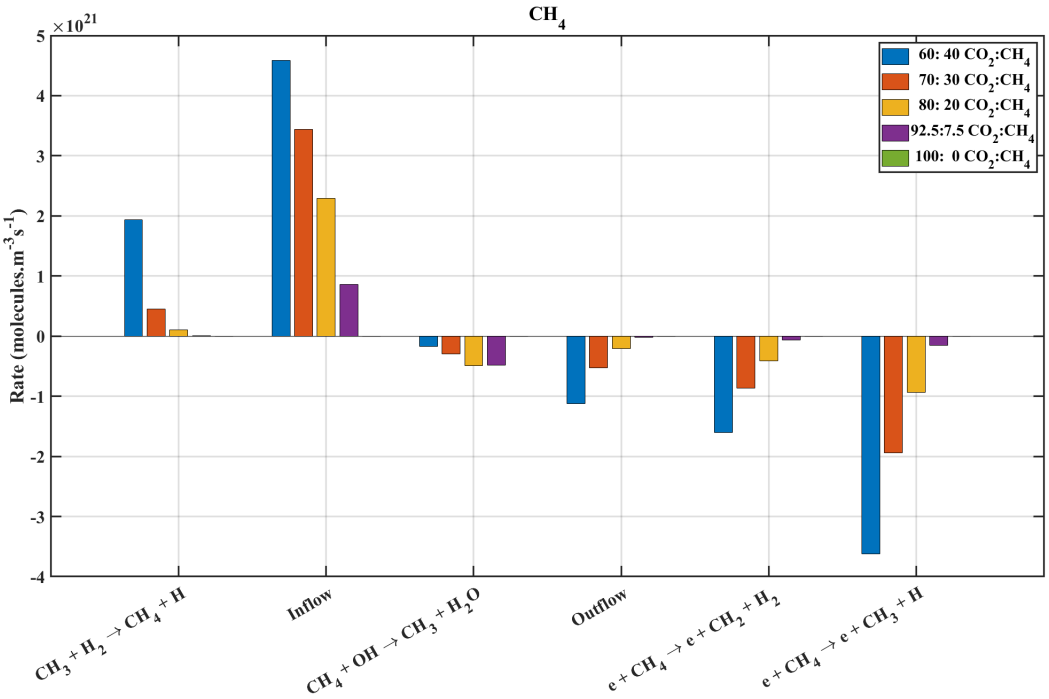

Figure 27: Evolution with initial mixture of the reaction rates of the main creation and destruction processes of CH_4 at pseudo-steady state in a 60:40 CO2:CH4 plasma at 1.85 sccm, 5 Torr. The positive rates represent the creation, the negative the destruction processes. Each initial mixture is plotted in a different color.

The processes creating and destroying CH_4 are simpler. A plot showing the reaction rates of the main CH_4 processes as a function of the initial mixture (at 5 Torr, 1.85 sccm) is shown on figure 27. Independently of the initial mixture, CH_4 is created by two processes: the inflow, and the back-reaction mechanism (12) ($CH_3 + H_2 \rightarrow CH_4 + H$). This process logically increases with CH_4 initial %, because more CH_3 and H_2 are available. The loss of CH_4 happens mostly through 4 mechanisms: outflow, the two electron impact dissociation processes and the reaction (25).

$$CH_4 + OH \rightarrow CH_3 + H_2O \tag{25}$$

This last process is the only direct oxidation process of CH_4. It is also the only one that is not linear with CH_4 initial %. This process producing water is also maximum in the 80:20 CO_2:CH_4 mixtures (where the water fraction is maximum). It would however be too simplistic to attribute the peak of H_2O solely to process (25).

Creation and loss processes of H_2O and OH

The most important processes for H_2O production are presented on figure 28. Water is created through 3 main processes in the steady state:

$$CH_3 + OH \rightarrow H_2O + CH_2 \tag{26}$$

$$H_2 + OH \rightarrow H_2O + H \tag{27}$$

$$CH_2O + OH \rightarrow H_2O + HCO \tag{28}$$

Out of these 3 processes, the last one is the only one being maximum for 80:20 CO_2:CH_4 mixture. The others are linear with the CH_4 admixture. The process (28) peaks at 80:20 because it is where the product of the density of OH times the density of CH_2O is maximum (OH decreases with increasing CH_4 percentage while CH_2O increases). Figure 29 shows the temporal evolution of the reactions leading to the equilibrium reached for OH and CH_2O in the 80:20 CO_2:CH_4 mixture (the figure describes the evolution of the rates in the reactor over time, from the plasma breakdown to the pseudo-steady state at the exit of the plasma). For each species, the top graph shows the evolution of the density over time. The bottom graph shows the reaction rates of the main reactions. The creation processes are plotted with plain lines and the destruction processes are plotted with dashed lines. The density of OH, plotted in the top left graph goes through a maximum (at 1ms) before oscillating toward its final values (i.e it is possible to tune the products by changing the plasma duration). OH is initially produced through:

$$CH_4 + O(^1D) \rightarrow CH_3 + OH \tag{13}$$

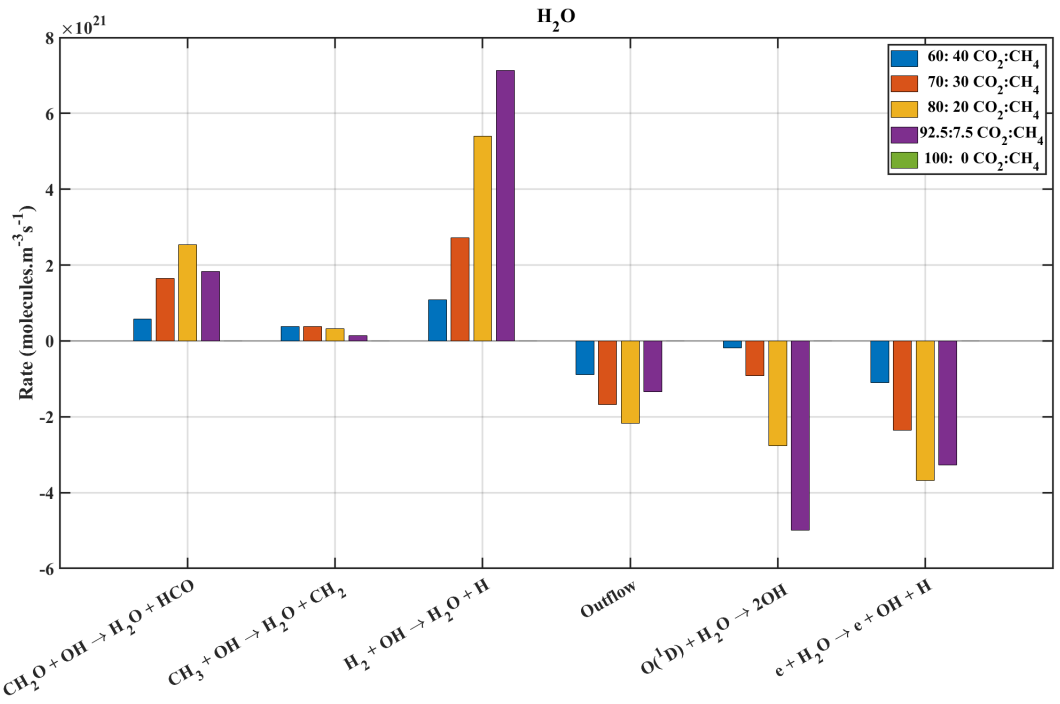

Figure 28: Evolution with initial mixture of the reaction rates of the main creation and destruction processes of H_2O at pseudo-steady state at 1.85 sccm, 5 Torr. The positive rates represent the creation, the negative the destruction processes. Each initial mixture is plotted in a different color.

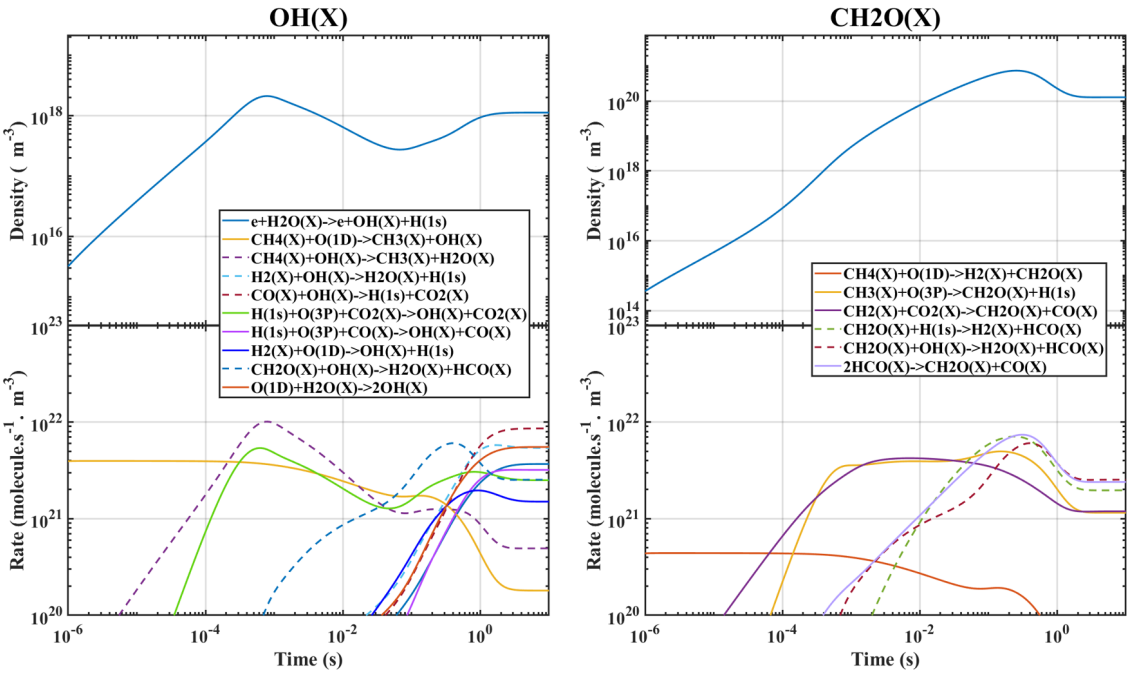

Figure 29: Top: Temporal evolution of the densities of OH (Left) and CH_2O (right) in a 80:20 CO_2:CH_4 mixture at 5 Torr and 1.85 sccm. t=0 is the break-down of the plasma. A pseudo-steady state is reached when the dissociation is compensated by the gas renewal. Bottom: Temporal evolution of the reaction rates of processes involving OH (left) and CH_2O (right). The creation processes of the concerned species are plotted in plain line, the loss processes are plotted in dashed line. t=0 correspond to the plasma break-down.

The rate coefficient of this reaction is taken from [71]. To the best of our knowledge, this production channel was not identified in any CO_2-CH_4 plasma model, but was put forward in [72] (which compared experiment and simulation for CH_4-O_2 mixtures in nanosecond discharges). In [72], process (13) was the most important loss channel of CH_4 (accounting for 40% of the loss), above electron impact dissociation (all electron impact channels sum up to 38%) despite the very high electric field and electron density of nanosecond discharges. The electron impact dissociation cross-section used in [72] is the one taken from [70], lower than the one used in this work, which could partly explain the difference with CH_4 dissociation in our work. The reaction of $O(^1D)$ with CH_3 (process (14)) was not taken into account in [72], which ultimately increased the amount of $O(^1D)$ available to react with CH_4, also explaining the difference. This however shows in another way the importance of the $O(^1D)$ state. Without it, the initial building up of OH and eventually the peak in the water fraction is difficult to explain. Process (13) builds up the OH density until 1ms. Between 1ms and 1s, the OH density is reduced because OH reacts with CH_2O and produces water (explaining the peak of water in the 80:20 CO_2:CH_4 mixture). Once enough water is accumulated, water and OH reach an equilibrium through 6 processes, 3 of them forming OH, the other 3 destroying it

$$O(^1D) + H_2O \rightarrow 2OH \quad (29)$$
$$e + H_2O \rightarrow e + OH + H \quad (30)$$
$$H + O + M \rightarrow OH + M \quad (31)$$
$$CO + OH \rightarrow CO_2 + H \quad (21)$$
$$H_2 + OH \rightarrow H_2O + H \quad (27)$$
$$CH_2O + OH \rightarrow H_2O + HCO \quad (28)$$

The most important ones are found on figure 28. This is only possible because enough CH_2O is available in the plasma.

Creation and loss processes of CH_2O

Similarly to OH, the density of CH_2O (plotted on the top right graph of figure 29), goes through a maximum around 0.1s. The density of CH_2O is initially built up by the reaction:

$$CH_4 + O(^1D) \rightarrow CH_2O + H_2 \quad (32)$$

This reaction was also identified in [72] and had a reaction rate about 10 times lower than the other channel involving CH_4 and $O(^1D)$ (13), which is similar to our observations. When CH_4 starts being dissociated enough (around 10^{-4}s), the CH_2O production is assured by :

$$CH_2 + CO_2 \rightarrow CH_2O + CO \quad (24)$$
$$CH_3 + O \rightarrow CH_2O + H \quad (33)$$
$$2HCO \rightarrow CH_2O + CO \quad (34)$$

These reactions later balance with water production (28), as seen above. Because these reactions are the one that build up the CH_2O density, their rate coefficients could be overestimated, explaining why the simulated CH_2O is overestimated compared to experimental observations. The rate coefficient of process (24) was taken from [56], but the rate coefficient proposed in [73] is 3 times lower. The rate coefficient used for reaction (33) is taken from [69] and is in good agreement with numerous other values available in literature. Finally, the rate coefficient of reaction(34) is taken from [56] and is the lowest value of the rate available in literature. The reaction (24) seems to be the only one whose rate coefficient would indeed be overestimated. Using a smaller rate coefficient would not lower the CH_2O density by a factor 4, this should be investigated in future work.

Creation and loss processes of H_2

The evolution of the main processes involving H_2 as a function of the initial mixture at 5 Torr, 1.85 sccm, are shown on figure 30. The majority of H_2 is produced by wall recombination of hydrogen atoms, highlighting the critical dependence of the model to the recombination probability γ_H. The rest of the hydrogen is mostly produced by

$$CH_2O + H \rightarrow H_2 + HCO \quad (35)$$

underlining the important role of CH_2O in our plasma. At low CH_4 percentage mixtures, the 3-body process H + OH + M is also a source of H_2. In these mixtures, the production of water through

$$H_2 + OH \rightarrow H_2O + H \quad (27)$$

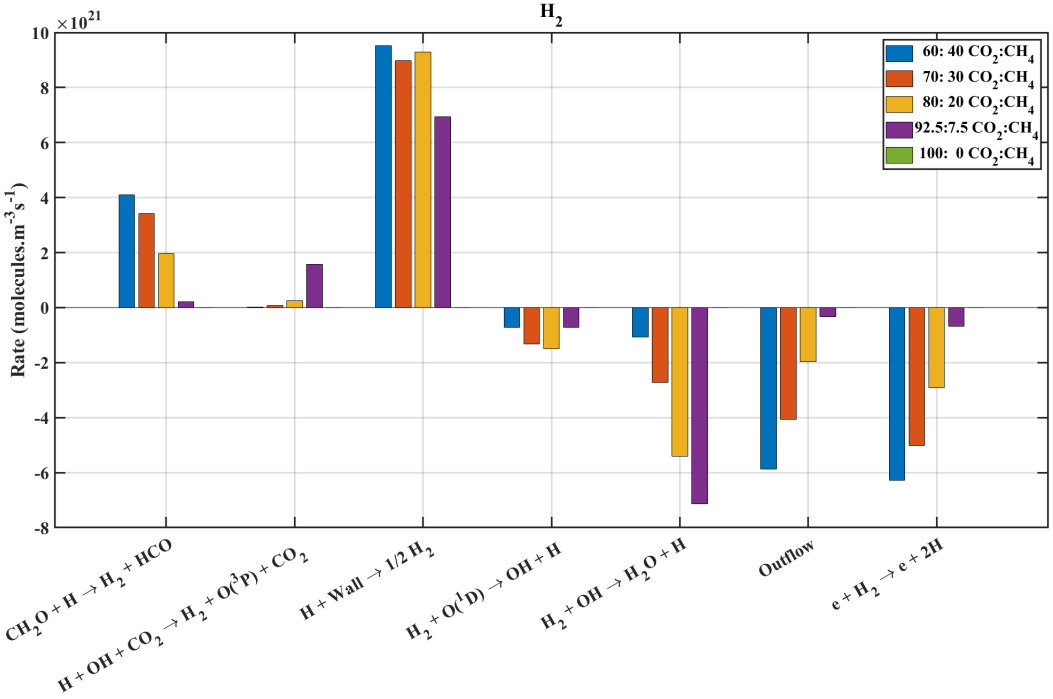

Figure 30: Evolution with initial mixture of the reaction rates of the main creation and destruction processes of H_2 at pseudo-steady state at 1.85 sccm, 5 Torr. The positive rates represent the creation, the negative the destruction processes. Each initial mixture is plotted in a different color.

is the main destruction channel of H_2. At high initial CH_4 percentages mixtures, H_2 is destroyed by outflow and electron impact. Finally, in all the conditions, the dissociation of H_2 through collision with $O(^1D)$ is non-negligible, representing about 10% of H_2 loss.

Creation and loss processes of $O(^1D)$

Throughout all the discussions before, $O(^1D)$ appeared to be a key species for the whole kinetic scheme. Though processes involving $O(^1D)$ are rarely the most important ones, processes involving $O(^1D)$ are found to significantly impact the final balances and densities for all mixtures and all pressures. It could be that H_2O does not appear important in other models simply because $O(^1D)$ reactions are not including preventing the formation of H_2O. The question of the production and loss of $O(^1D)$ must be addressed. Figure 31 shows the evolution of the reaction rates of processes involving $O(^1D)$ as a function of the initial mixture at 5 Torr, 1.85 sccm. In pure CO_2 plasmas, $O(^1D)$ is produced not only through electron impact dissociation of CO_2, but also through electron impact dissociation of O_2 and through electronic excitation of $O(^3P)$. Because of the very low level of atomic O and O_2 in CO_2-CH_4 plasmas, these last two channels are negligible in CO_2-CH_4 plasmas and $O(^1D)$ is produced only by electron impact dissociation of CO_2. In pure CO_2 plasmas, $O(^1D)$ is mainly lost by collisional quenching with CO_2. This channel is not the dominant loss of $O(^1D)$ anymore when the initial CH_4 percentage is higher than 10. Apart from simple quenching, $O(^1D)$ is lost through 3 main channels:

$$CH_3 + O(^1D) \rightarrow CO + H_2 + H \quad (14)$$

$$H_2O + O(^1D) \rightarrow 2OH \quad (29)$$

$$H_2 + O(^1D) \rightarrow OH + H \quad (36)$$

with the first one being probably an effective process, i.e grouping several processes. The branching between these channels depends on the rate coefficient chosen for the first one which is unknown and therefore just an assumption in this work. With the rate coefficient chosen here, 1/3rd of the $O(^1D)$ at 20% initial CH_4 is lost in ($O(^1D)$ + H_2O), 1/3 by collisional quenching and the other third is split between H_2+$O(^1D)$ and CH_3+$O(^1D)$. When increasing the initial CH_4 percentage to 30%, the loss of $O(^1D)$ is more or less equally parted between the 4 channels. At 40 % initial CH_4, 2/3rd of the $O(^1D)$ is lost through process (14), highlighting the critical stake of obtaining through other methods a value of this rate to clarify the importance of the interaction between CH_3 and $O(^1D)$ and therefore obtain a better picture of a CO_2:CH_4 plasma.

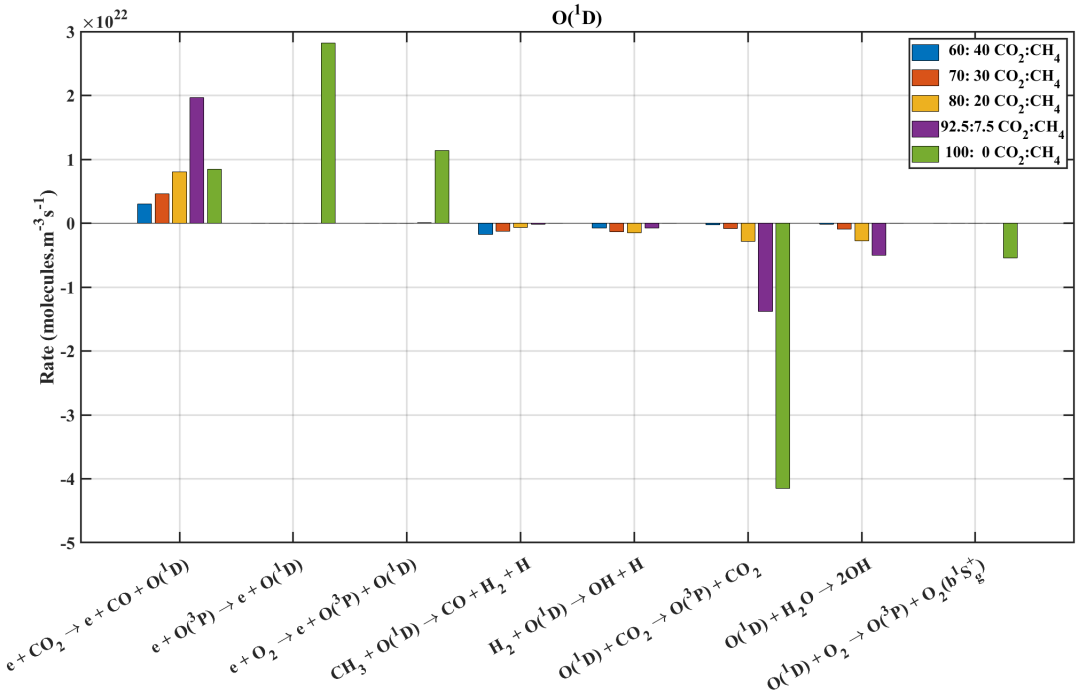

Figure 31: Evolution with initial mixture of the reaction rates of the main creation and destruction processes of O(^{1}D) at pseudo-steady state at 1.85 sccm, 5 Torr. The positive rates represent the creation, the negative the destruction processes. Each initial mixture is plotted in a different color.

7 Conclusions

A low pressure glow discharge has been set up and used to validate a 0D kinetic model for CO_2-CH_4 plasmas, using the LoKI simulation tool. The model takes into account a relatively simple chemistry including only molecules with at most one carbon atom, as well as CH_4 and its derivatives. A rather good agreement has been found between the model predictions. The simulations capture accurately the main features and trends observed experimentally, allowing to use the model to gain insights on the key processes of CO_2-CH_4 plasmas. It has been shown that in our conditions, electronic impact dissociation of CO_2 and CH_4 are the main channels to produce the major products, CO and H_2, but that some highly reactive species also play an important role. The back-reaction combining CO and OH to form CO_2 and atomic H seems to be the reason behind the limited conversion of CO_2 at low CH_4 percentages in the initial mixtures. O(^{1}D) and OH oxidation of CH_4 have shown to be important loss mechanisms of CH_4, emphasizing the role of excited states in the chemistry of CO_2-CH_4 plasma. The parametric study performed here strongly suggest that the interaction between O(^{1}D) and CH_3 through

$$CH_3 + O(^1D) \rightarrow CO + H_2 + H$$

is necessary to explain the observed level of conversion of CH_4 and the production of H_2. The high rate coefficient used in this work however suggest that this reaction is an effective way of describing a more complex sequence of elementary processes. It would, however, be important to succeed in directly measuring the densities of CH_3 or O(^{1}D) in order to provide further clues as to the mechanisms potentially hidden by this actual process. It would be also important to quantify the reaction rates of the CO(a3Π) state (critical in pure CO_2 plasmas) with hydrogenated species. The comparison of the experimental and simulated reduced electric field sheds light on the charge creation in the CO_2-CH_4 plasma and on the dependency of the main ion densities to the single charge transfer reaction $CH_4 + CH_4^+ \rightarrow CH_5^+ + CH_3$. In our model, excluding this single reaction from the scheme leads to CH_4^+ being the main ion and to a significant improvement of the self-consistent calculated E/N. However, further experimental investigation are needed to determine the main ion in the CO_2-CH_4 discharge. For DRM purposes, it would be useful to have a better understanding of the processes taking place on the surfaces because as shown, they could be of interest also to produce value-added chemicals such as C_2H_6. In part II of this paper [27], a CeO_2 pellet is exposed to the plasma studied here. CeO_2 is a common support for active phase of catalyst for DRM as well as for methanation. The detailed description of the gas phase as it has been achieved in this Part I of the paper provides all useful parameters (E/N, gas temperature, densities of all main species, etc...) to analyse the species forming onto the surface of CeO_2. The good agreement between simulation and experiments shown here still leaves room for improvements. Firstly, the vibrational excitation

of CO_2 and CO could be taken into account in the chemistry part. Secondly, though it seems that they are not essential for CO_2-CH_4 chemistry in our conditions, the larger hydrocarbons species may be taken into account in the model as it is not so clear whether their influence on the chemistry is comparable to the one of excited states or not. The quantitative comparison of experiment and model appears to be crucial to bring insights about a chemistry as complex as the one of CO_2-CH_4 plasmas.

Statements and Declarations

All authors certify that they have no affiliations with or involvement in any organization or entity with any financial interest or non-financial interest in the subject matter or materials discussed in this manuscript

Ethical Approval (applicable for both human and/ or animal studies. Ethical committees, Internal Review Boards and guidelines followed must be named. When applicable, additional headings with statements on consent to participate and consent to publish are also required)
this declaration is not applicable for the work proposed in this paper.

Competing interests (always applicable and includes interests of a financial or personal nature)
No, I declare that the authors have no competing interests as defined by Springer, or other interests that might be perceived to influence the results and/or discussion reported in this paper.

Authors' contributions (applicable for submissions with multiple authors)
E.B. did the measurement, developed the kinetic scheme and wrote the paper
C.A.G.S. contributed to experiment
T.S. and V.G. developed the code
V.P. discussed the chemistry
O.G. supervised the work
All authors reviewed the manuscript

Funding (details of any funding received)
This work was partially supported by the Agence Nationale de la Recherche (ANR, Investissement d'Avenir program), under project ANR-18-EURE-0014. This work was partially supported by the Portuguese FCT-Fundacao para a Ciencia e a Tecnologia, under projects UIDB/50010/2020, UIDP/50010/2020, PTDC/FIS-PLA/1616/2021, EXPL/FIS-PLA/0076/2021. This project has received funding from the European Union's Horizon 2020 research and innovation programme under the Marie Skłodowska-Curie grant agreement No. 813393.

Availability of data and materials (a statement on how any datasets used can be accessed)
All data presented in this work will be made available upon request to the corresponding author.

References

[1] Centi and Perathoner. "Opportunities and prospects in the chemical recycling of carbon dioxide to fuels". In: *Catalysis Today* 148.3-4 (November 2009), pp. 191–205. DOI: https://doi.org/10.1016/j.cattod.2009.07.075 (cit. on p. 2).

[2] R.Snoeckx and A.Bogaerts. "Plasma technology – a novel solution for CO2 conversion?" In: *Chemical Society Reviews* 46 (2017), pp. 5805–5863. DOI: 10.1039/C6CS00066E (cit. on p. 2).

[3] J Amouroux and P Siffert. "Carbon dioxide: a raw material and a future chemical fuel for a sustainable energy industry". In: *IOP Conference Series: Materials Science and Engineering* 19 (Mar. 2011), p. 012001. DOI: 10.1088/1757-899x/19/1/012001. URL: https://doi.org/10.1088/1757-899x/19/1/012001 (cit. on p. 2).

[4] Alexander Fridman. *Plasma Chemistry*. Cambridge University Press, 2009. DOI: https://doi.org/10.1017/CBO9780511546075 (cit. on p. 2).

[5] W.J.Witteman. *The CO_2 laser*. Springer, 1986 (cit. on p. 2).

[6] Ana Sofia Morillo-Candas, Vasco Guerra, and Olivier Guaitella. "Time Evolution of the Dissociation Fraction in rf CO2 Plasmas: Impact and Nature of Back-Reaction Mechanisms". In: *The Journal of Physical Chemistry C* 124.32 (2020), pp. 17459–17475. DOI: 10.1021/acs.jpcc.0c03354 (cit. on p. 2).

[7] L.D.Pietanza, O.Guaitella, V.Aquilanti, et al. "Advances in non-equilibrium CO2 plasma kinetics: a theoretical and experimental review". In: *Eur. Phys. J. D* 75.237 (2021). DOI: https://doi.org/10.1140/epjd/s10053-021-00226-0 (cit. on p. 2).

[8] V.Schulz-von der Gathen et al. "Plasma Sources Science and Technology Diagnostic studies of species concentrations in a capacitively coupled RF plasma containing CH4-H2-Ar". In: *Plasma Sources Sci. Technol.* 10 (2001), p. 530. DOI: https://doi.org/10.1088/0963-0252/10/3/318 (cit. on p. 2).

[9] J.R.Fincke et al. "Plasma Thermal Conversion of Methane to Acetylene". In: *Plasma Chemistry and Plasma Processing* 22 (1 2002). DOI: 10.1023/a:1012944615974 (cit. on pp. 2, 24).

[10] K Hassouni et al. "Investigation of chemical kinetics and energy transfer in a pulsed microwave H2/CH4 plasma". In: *Plasma Sources Science and Technology* 10.1 (Jan. 2001), pp. 61–75. DOI: 10.1088/0963-0252/10/1/309. URL: https://doi.org/10.1088/0963-0252/10/1/309 (cit. on p. 2).

[11] M.Scapinello et al. "Conversion of CH4 /CO2 by a nanosecond repetitively pulsed discharge". In: *J. Phys. D: Appl. Phys.* 49 (2016), p. 075602. DOI: https://doi.org/10.1088/0022-3727/49/7/075602 (cit. on pp. 2, 6).

[12] S.Zhang, X.Zeng, H. Bai, et al. "Optical emission spectroscopy measurement of plasma parameters in a nanosecond pulsed spark discharge for CO_2-CH_4 dry reforming". In: *Spectrochimica Acta Part A: Molecular and Biomolecular Spectrocscopy* 267 (2022), p. 120590. DOI: https://doi.org/10.1016/j.saa.2021.120590 (cit. on p. 2).

[13] H.Li et al. "Optical and Mass Spectrometric Measurements of the CH4-CO2 Dry Reforming Process in a Low Pressure, Very High Density, and Purely Inductive Plasma". In: *J. Phys. Chem. A* 124 (2020), 7271-7282. DOI: https://dx.doi.org/10.1021/acs.jpca.0c04033 (cit. on p. 2).

[14] S. Van Alphen et al. "Effect of N2 on CO2-CH4 conversion in a gliding arc plasmatron: Can this major component in industrial emissions improve the energy efficiency?" In: *Journal of CO2 Utilization* 54 (2021), p. 101767. DOI: https://doi.org/10.1016/j.jcou.2021.101767 (cit. on pp. 2, 6).

[15] Seigo Kameshima et al. "Pulsed dry methane reforming in plasma-enhanced catalytic reaction". In: *Catalysis Today* 256 (2015). Plasmas for enhanced catalytic processes (ISPCEM 2014), pp. 67–75. ISSN: 0920-5861. DOI: https://doi.org/10.1016/j.cattod.2015.05.011 (cit. on p. 2).

[16] L.Wang and others. "One-Step Reforming of CO2 and CH4 into High-Value Liquid Chemicals and Fuels at Room Temperature by Plasma-Driven Catalysis". In: *Angewandte Chemie* 56 (2017), pp. 13679–13683. DOI: http://dx.doi.org/10.1002/anie.201707131 (cit. on p. 2).

[17] Annemie Bogaerts et al. "The 2020 plasma catalysis roadmap". In: *Journal of Physics D: Applied Physics* 53.44 (Aug. 2020), p. 443001. DOI: 10.1088/1361-6463/ab9048. URL: https://doi.org/10.1088/1361-6463/ab9048 (cit. on p. 2).

[18] Annemie Bogaerts et al. "Foundations of plasma catalysis for environmental applications". In: *Plasma Sources Science and Technology* 31.5 (May 2022), p. 053002. DOI: 10.1088/1361-6595/ac5f8e. URL: https://doi.org/10.1088/1361-6595/ac5f8e (cit. on p. 2).

[19] A. Bogaerts et al. "Plasma based CO_2 and CH_4 conversion: A modeling perspective". In: *Plasma Process Polym* 14 (2016). DOI: 10.1002/ppap.201600070 (cit. on p. 2).

[20] C. De Bie et al. "The Dominant Pathways for the Conversion of Methane into Oxygenates and Syngas in an Atmospheric Pressure Dielectric Barrier Discharge". In: *J. Phys. Chem. C* 119 (2015), 2331-22350. DOI: http://dx.doi.org/10.1021/acs.jpcc.5b06515 (cit. on pp. 2, 20, 21, 23, 24, 26–28).

[21] W.Wang et al. "Modeling Plasma-based CO2 and CH4 Conversion in Mixtures with N2, O2, and H2O: The Bigger Plasma Chemistry Picture". In: *J. Phys. Chem. C* 122.16 (2018), pp. 8704–8723. DOI: https://doi.org/10.1021/acs.jpcc.7b10619 (cit. on p. 2).

[22] C.Bai. "Numerical investigation on the CH4/CO2 nanosecond pulsed dielectric barrier discharge plasma at atmospheric pressure". In: *AIP Advances* 9 (2019), p. 035023. DOI: 10.1063/1.5063519 (cit. on pp. 2, 12, 20, 23, 26–28).

[23] Jie Pan et al. "Numerical modeling and mechanism investigation of nanosecond-pulsed DBD plasma catalytic CH_4 dry reforming". In: *J. Phys. D: Appl. Phys* 55 (2022), p. 035202. DOI: https://doi.org/10.1088/1361-6463/ac2ad8 (cit. on p. 2).

[24] Mingrui Zhu et al. "Surface induced gas-phase redistribution effects in plasma-catalytic dry reforming of methane: numerical investigation by fluid modeling". In: *J. Phys. D: Appl. Phys* 55 (2022), p. 355201. DOI: https://doi.org/10.1088/1361-6463/ac74f7 (cit. on p. 2).

[25] Danhua Mei et al. “CH4 reforming with CO2 using a nanosecond pulsed dielectric barrier discharge plasma”. In: *Journal of CO2 Utilization* 62 (2022), p. 102073. ISSN: 2212-9820. DOI: https://doi.org/10.1016/j.jcou.2022.102073. URL: https://www.sciencedirect.com/science/article/pii/S2212982022001925 (cit. on pp. 2, 26).

[26] A F Silva et al. “A reaction mechanism for vibrationally-cold low-pressure CO2 plasmas”. In: *Plasma Sources Science and Technology* 29.12 (Dec. 2020), p. 125020. DOI: 10.1088/1361-6595/abc818 (cit. on pp. 2, 10–13, 19, 25).

[27] Carolina A. Garcia-Soto et al. “CO_2/CH_4 plasma glow discharge. Part II: Study of plasma catalysis interaction on CeO_2”. In: *Plasma Sources Science and Technology* ("submitted") (cit. on pp. 2, 6, 24, 29, 35).

[28] Y.Du et al. “CO(B1Sigma–>A1Pi) Angstrom System for Gas Temperature Measurements in CO2 Containing Plasmas”. In: *Plasma Chem Plasma Process* 37 (2017), pp. 29–41. DOI: DOI10.1007/s11090-016-9759-5 (cit. on p. 4).

[29] B L M Klarenaar et al. “Time evolution of vibrational temperatures in a CO2 glow discharge measured with infrared absorption spectroscopy”. In: *Plasma Sources Science and Technology* 26.11 (Oct. 2017), p. 115008. DOI: 10.1088/1361-6595/aa902e (cit. on p. 4).

[30] T. Silva et al. “Dynamics of Gas Heating in the Afterglow of Pulsed CO2 and CO2–N2 Glow Discharges at Low Pressure”. In: *Plasma Chemistry and Plasma Processing* 40.3 (Jan. 2020), pp. 713–725. DOI: 10.1007/s11090-020-10061-7. URL: https://doi.org/10.1007/s11090-020-10061-7 (cit. on p. 5).

[31] A.M. Ghorbanzadeh and H. Modarresi. “Carbon dioxide reforming of methane by pulsed glow discharge at atmospheric pressure: The effect of pulse compression”. In: *J. Appl. Phys.* 101 (2007), p. 123303. DOI: https://doi.org/10.1063/1.2745425 (cit. on p. 6).

[32] A S Morillo-Candas et al. “Oxygen atom kinetics in CO2 plasmas ignited in a DC glow discharge”. In: *Plasma Sources Science and Technology* 28.7 (July 2019), p. 075010. DOI: 10.1088/1361-6595/ab2b84 (cit. on pp. 8, 10, 13, 22, 27).

[33] A. Tejero-del-Caz. “The LisbOn KInetics Boltzmann solver”. In: *Plasma Sources Sci. Technol.* 28 (2019), p. 043001. DOI: https://doi.org/10.1088/1361-6595/ab0537 (cit. on pp. 9–11).

[34] A Kramida et al. *NIST Atomic Spectra Database (ver. 5.10)*. 2022. URL: https://physics.nist.gov/asd. National Institute of Standards and Technology, Gaithersburg, MD. (Cit. on p. 10).

[35] J. Bittner et al. “Quenching of two-photon-excited H(3s, 3d) and O(3p 3P2,1,0) atoms by rare gases and small molecules”. In: *Chemical Physics Letters* 143.6 (1988), pp. 571–576. ISSN: 0009-2614. DOI: https://doi.org/10.1016/0009-2614(88)87068-4 (cit. on p. 10).

[36] K Niemi, V Schulz-von der Gathen, and H F Döbele. “Absolute atomic oxygen density measurements by two-photon absorption laser-induced fluorescence spectroscopy in an RF-excited atmospheric pressure plasma jet”. In: *Plasma Sources Science and Technology* 14.2 (Apr. 2005), pp. 375–386. DOI: 10.1088/0963-0252/14/2/021 (cit. on p. 10).

[37] T. Tsutsumi et al. “Investigation of the radially resolved oxygen dissociation degree and local mean electron energy in oxygen plasmas in contact with different surface materials”. In: *Journal of Applied Physics* 121.14 (2017), p. 143301. DOI: 10.1063/1.4979855 (cit. on p. 10).

[38] A. Tejero-del-Caz. “On the quasi-stationary approach to solve the electron Boltzmann equation in pulsed plasmas”. In: *Plasma Sources Sci. Technol.* 30 (2021), p. 065008. DOI: https://doi.org/10.1088/1361-6595/abf858 (cit. on pp. 10, 11).

[39] Marija Grofulović, Luís L Alves, and Vasco Guerra. “Electron-neutral scattering cross sections for CO2: a complete and consistent set and an assessment of dissociation”. In: *Journal of Physics D: Applied Physics* 49 (2016), p. 395207. DOI: doi:10.1088/0022-3727/49/39/395207 (cit. on pp. 11, 16).

[40] G Gousset et al. “Electron and heavy-particle kinetics in the low pressure oxygen positive column”. In: *Journal of Physics D: Applied Physics* 24.3 (Mar. 1991), pp. 290–300. DOI: 10.1088/0022-3727/24/3/010 (cit. on p. 11).

[41] Luués Lemos Alves et al. “Electron scattering cross sections for the modelling of oxygen-containing plasmas”. In: *The European Physical Journal D* 70.6 (June 2016). DOI: 10.1140/epjd/e2016-70102-1. URL: https://doi.org/10.1140/epjd/e2016-70102-1 (cit. on p. 11).

[42] Polina Ogloblina et al. “Electron impact cross sections for carbon monoxide and their importance in the electron kinetics of CO2–CO mixtures”. In: *Plasma Sources Science and Technology* 29.1 (Dec. 2019), p. 015002. DOI: 10.1088/1361-6595/ab4e72. URL: https://dx.doi.org/10.1088/1361-6595/ab4e72 (cit. on p. 11).

[43] Maik Budde et al. “Electron-neutral collision cross sections for H_2O: I. Complete and consistent set”. In: *Journal of Physics D: Applied Physics* 55.44 (Sept. 2022), p. 445205. DOI: 10.1088/1361-6463/ac8da3 (cit. on p. 11).

[44] D.Bouwman et al. “Neutral dissociation of methane by electron impact and a complete and consistent cross section set”. In: *Plasma Sources Sci. Technol.* 30 (2021), p. 075012. DOI: https://doi.org/10.1088/1361-6595/ac0b2b (cit. on pp. 11, 16, 17, 27).

[45] L L Alves. “The IST-LISBON database on LXCat”. In: *Journal of Physics: Conference Series* 565.1 (Dec. 2014), p. 012007. DOI: 10.1088/1742-6596/565/1/012007. URL: https://dx.doi.org/10.1088/1742-6596/565/1/012007 (cit. on p. 11).

[46] Tom Butterworth et al. “Plasma induced vibrational excitation of CH_4—a window to its mode selective processing”. In: *Plasma Sources Science and Technology* 29.9 (Sept. 2020), p. 095007. DOI: 10.1088/1361-6595/aba1c9 (cit. on p. 12).

[47] D.F. Starr et al. “Vibrational deactivation of carbon monoxide by hydrogen and nitrogen from 100 to 650 °K”. In: *J. Chem. Phys.* 61 (1974), p. 5421. DOI: https://doi.org/10.1063/1.1681897 (cit. on p. 12).

[48] Roger C. Millikan. “Vibration—Vibration Energy Exchange between Carbon Monoxide and Methane”. In: *J. Chem. Phys.* 43 (1965), p. 1439. DOI: https://doi.org/10.1063/1.1696952 (cit. on p. 12).

[49] C. Fromentin et al. “Validation of non-equilibrium kinetics in CO2-N2 plasmas”. In: 32 (2023), p. 024001 (cit. on p. 12).

[50] Tiago Silva et al. “Modeling the time evolution of the dissociation fraction in low-pressure CO2 plasmas”. In: *Journal of CO_2 Utilization* 53 (2021), p. 101719. DOI: https://doi.org/10.1016/j.jcou.2021.101719 (cit. on p. 12).

[51] Joseph Oakland Hirschfelder, Charles F Curtiss, and R Byron Bird. “Molecular theory of gases and liquids”. In: *Molecular theory of gases and liquids* (1964) (cit. on p. 13).

[52] G. Cartry A.Rousseau and X.Duten. “Surface recombination of hydrogen atoms studied by a pulsed plasma excitation technique”. In: *Journal of Applied Physics* 89 (2001), p. 2074. DOI: https://doi.org/10.1063/1.1325000 (cit. on pp. 13, 22).

[53] K.E.Shuler and K.J.Laidle. “The Kinetics of Heterogeneous Atom and Radical Reactions. I. The Recombination of Hydrogen Atoms on Surfaces”. In: *J. Chem. Phys.* 17 (1949), p. 1212. DOI: https://doi.org/10.1063/1.1747144 (cit. on p. 13).

[54] Luis L. Alves and Antonio Tejero-del-Caz. “Charged-particle transport models for global models”. In: *Plasma Sources Science and Technology* (Apr. 2023). DOI: 10.1088/1361-6595/acce96. URL: https://doi.org/10.1088/1361-6595/acce96 (cit. on p. 13).

[55] C. Makochekanwa. “Experimental observation of neutral radical formation from CH4 by electron impact in the threshold region”. In: *Physical Review A* 74 (2006), p. 042704. DOI: http://dx.doi.org/10.1103/PhysRevA.74.042704 (cit. on p. 16).

[56] W. Tsang and R.F Hampson. “Chemical kinetic data base for combustion chemistry. Part I. Methane and related compounds”. In: *J. Phys. Chem. Ref. Data* 15 (1986) (cit. on pp. 17, 26, 33).

[57] D.L. Baulch et al. “Evaluated kinetic data for combustion modeling: Supplement I”. In: *J. Phys. Chem.* 23 (1994), p. 847 (cit. on p. 17).

[58] J. Warnatz. *Combustion Chemistry: Rate coefficients in the C/H/O system.* Springer - Verlag, 1984 (cit. on p. 17).

[59] D.Smith and N.G.Adams. “Reaction of simple hydrocarbon ions with molecules at thermal energies”. In: *Plasma Sources Sci. Technol.* 23 (2 1977), pp. 123–135. DOI: https://doi.org/10.1016/0020-7381(77)80094-6 (cit. on pp. 20, 21).

[60] J. K. Kim and W. T. Huntress. “Ion cyclotron resonance studies on the reaction of H2+ and D2+ ions with various simple molecules and hydrocarbons”. In: *The Journal of Chemical Physics* 62.7 (1975), pp. 2820–2825. DOI: 10.1063/1.430817 (cit. on p. 20).

[61] D. Smith and N.G. Adams. “Reaction of simple hydrocarbon ions with molecules at thermal energies”. In: *International Journal of Mass Spectrometry and Ion Physics* 23.2 (1977), pp. 123–135. ISSN: 0020-7381. DOI: https://doi.org/10.1016/0020-7381(77)80094-6. URL: https://www.sciencedirect.com/science/article/pii/0020738177800946 (cit. on p. 20).

[62] L.A. Viehland and E.A. Mason. “Transport Properties of Gaseous Ions over a Wide Energy Range, IV”. In: *Atomic Data and Nuclear Data Tables* 60.1 (1995), pp. 37–95. ISSN: 0092-640X. DOI: https://doi.org/10.1006/adnd.1995.1004. URL: https://www.sciencedirect.com/science/article/pii/S0092640X85710042 (cit. on p. 20).

[63] F.H.Field, J.L.Franklin, and F.W.Lampe. "Reactions of Gaseous Ions. I. Methane and Ethylene". In: *J. Am. Chem. Soc.* 79 (10 1957), pp. 2419–2429. DOI: https://doi.org/10.1021/ja01567a020 (cit. on p. 21).

[64] Michael Henchman et al. "The mechanism of the reaction CH+4 + CH4 = CH+5 + CH3 as a function of energy: rate constants and product distributions for the reactions of CH+4 + CD4 and CD+4 + CH4 at 80 and 300 K". In: *International Journal of Mass Spectrometry and Ion Processes* 92 (1989), pp. 15–36. ISSN: 0168-1176. DOI: https://doi.org/10.1016/0168-1176(89)83016-2. URL: https://www.sciencedirect.com/science/article/pii/0168117689830162 (cit. on p. 21).

[65] G V Pokrovskiy, N A Popov, and S M Starikovskaia. "Fast gas heating and kinetics of electronically excited states in a nanosecond capillary discharge in CO2". In: *Plasma Sources Science and Technology* 31.3 (Mar. 2022), p. 035010. DOI: 10.1088/1361-6595/ac5102. URL: https://doi.org/10.1088/1361-6595/ac5102 (cit. on p. 23).

[66] Ana Sofia Morillo-Candas, Vasco Guerra, and Olivier Guaitella. "Time Evolution of the Dissociation Fraction in rf CO2 Plasmas: Impact and Nature of Back-Reaction Mechanisms". In: *The Journal of Physical Chemistry C* 124.32 (2020), pp. 17459–17475. DOI: 10.1021/acs.jpcc.0c03354 (cit. on p. 25).

[67] Jing-Lin Liu et al. "Mechanism study on gliding arc (GA) plasma reforming: A combination approach of experiment and modeling". In: *Plasma Processes and Polymers* 19.12 (Aug. 2022), p. 2200077. DOI: 10.1002/ppap.202200077. URL: https://doi.org/10.1002/ppap.202200077 (cit. on p. 26).

[68] Emelie Cleiren et al. "Dry Reforming of Methane in a Gliding Arc Plasmatron: Towards a Better Understanding of the Plasma Chemistry". In: *ChemSusChem* 10.20 (2017), pp. 4025–4036. DOI: https://doi.org/10.1002/cssc.201701274 (cit. on p. 26).

[69] D. L. Baulch et al. "Evaluated Kinetic Data for Combustion Modelling". In: *Journal of Physical and Chemical Reference Data* 21.3 (May 1992), pp. 411–734. DOI: 10.1063/1.555908. URL: https://doi.org/10.1063/1.555908 (cit. on pp. 26, 33).

[70] R K Janev et al. "Cross sections and rate coefficients for electron-impact ionization of hydrocarbon molecules". In: (Oct. 2001). URL: https://www.osti.gov/etdeweb/biblio/20234432 (cit. on pp. 27, 33).

[71] R. Atkinson et al. "Evaluated Kinetic and Photochemical Data for Atmospheric Chemistry: Supplement IV. IUPAC Subcommittee on Gas Kinetic Data Evaluation for Atmospheric Chemistry". In: *Journal of Physical and Chemical Reference Data* 21.6 (Nov. 1992), pp. 1125–1568. DOI: 10.1063/1.555918. URL: https://doi.org/10.1063/1.555918 (cit. on p. 33).

[72] J. Lefkowitz. "Species and temperature measurements of methane oxidation in a nanosecond repetitively pulsed discharge". In: *Phil. Trans. R. Soc A* 373 (2015), p. 20140333. DOI: https://dx.doi.org/10.1098/rsta.2014.0333 (cit. on p. 33).

[73] David C. Darwin and C. Bradley Moore. "Reaction rate constants (295K) for CH2 with H2S, SO2 and NO2: upper bounds for rate constants with less reactive partners". In: *J. Phys. Chem.* (1995) (cit. on p. 33).